J. Fluid Mech. (2018), *vol.* 853, *pp.* 171–204. © Cambridge University Press 2018
This is an Open Access article, distributed under the terms of the Creative Commons Attribution licence (http://creativecommons.org/licenses/by/4.0/), which permits unrestricted re-use, distribution, and reproduction in any medium, provided the original work is properly cited.
doi:10.1017/jfm.2018.537

Confinement effects on regular–irregular transition in shock-wave–boundary-layer interactions

Ilan J. Grossman[1,†] **and Paul J. K. Bruce**[1]

[1]Department of Aeronautics, Imperial College London, London SW7 2AZ, UK

(Received 20 August 2017; revised 22 May 2018; accepted 30 June 2018; first published online 22 August 2018)

An oblique shock wave is generated in a Mach 2 flow at a flow deflection angle of 12°. The resulting shock-wave–boundary-layer interaction (SWBLI) at the tunnel wall is observed. A novel traversable shock generator allows the position of the SWBLI to be varied relative to a downstream expansion fan. The relationship between the SWBLI, the expansion fan and the wind tunnel arrangement is studied. Schlieren photography, surface oil flow visualisation, particle image velocimetry and high-spatial-resolution wall pressure measurements are used to investigate the flow. It is observed that stream-normal movement of the shock generator downwards (towards the floor and hence the point of shock reflection) is accompanied by (1) growth in the streamwise extent of the shock-induced boundary layer separation, (2) upstream movement of the shock-induced separation point while the reattachment point remains nearly fixed, (3) an increase in separation shock strength and (4) transition between regular and irregular (Mach) reflection without an increase in incident shock strength. The role of free interaction theory in defining the separation shock angle is considered and shown to be consistent with the present measurements over a short streamwise extent. An SWBLI representation is proposed and reasoned which explains the apparent increase in separation shock strength that occurs without an increase in incident shock strength.

Key words: boundary layer separation, high-speed flow, shock waves

1. Introduction

Shock-wave–boundary-layer interactions (SWBLIs) are encountered in many internal and external compressible flows, and can be found across a wide range of applications from gas dynamic lasers to aircraft. Where they occur, SWBLIs impose a strong adverse pressure gradient on the boundary layer. This adverse pressure gradient can lead to flow unsteadiness, distortion and separation. Flow separation can have a large and direct impact on the operability of a given application.

† Email address for correspondence: ilan@caltech.edu

https://doi.org/10.1017/jfm.2018.537 Published online by Cambridge University Press

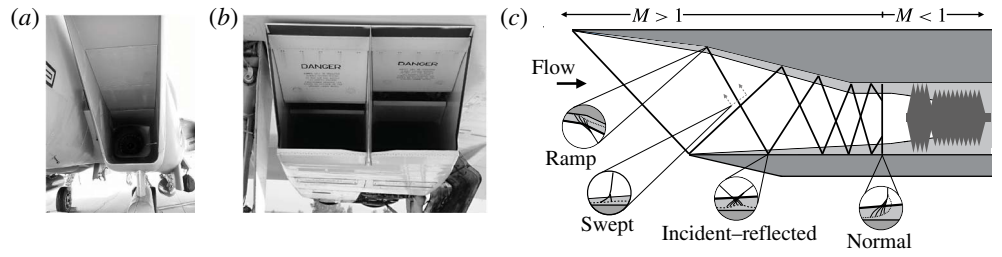

FIGURE 1. (*a*,*b*) Examples of the rectangular supersonic compression intakes of (*a*) the McDonnell Douglas F-15 Eagle (DAPM 2016) and (*b*) the Aérospatiale–BAC Concorde (Concorde-SST 2002). (*c*) Simplified schematic diagram showing the various types of SWBLIs.

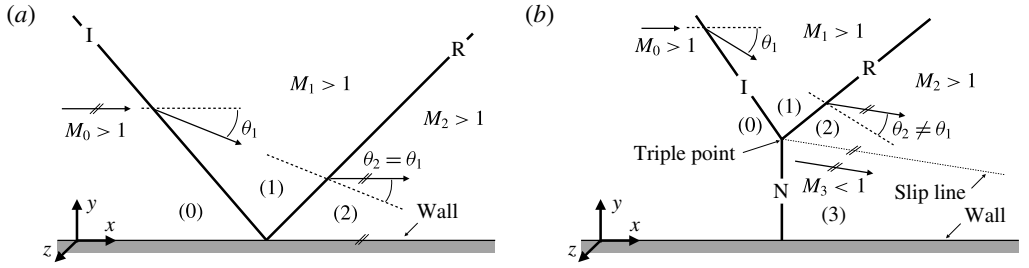

FIGURE 2. Types of shock reflection: (*a*) regular reflection (RR); (*b*) irregular or Mach reflection (MR).

Shock-wave–boundary-layer interactions can take on a variety of different forms dependent upon the type of shock wave (e.g. normal, oblique), the application geometry (e.g. axisymmetric, two-dimensional, three-dimensional) and the flow conditions at the point of the interaction (e.g. laminar or turbulent boundary layer). Figure 1(*c*) shows a range of SWBLI types occurring within a supersonic compression inlet (e.g. figure 1*a*,*b*), which is one of the most commonly studied applications (Longley & Greitzer 1992; Smart 2001; Ogawa & Babinsky 2006; Babinsky & Ogawa 2008; Babinsky, Oorebeek & Cottingham 2013; Loth *et al.* 2013).

The characteristics of an SWBLI can be further defined by the shock strength. If the shock strength were increased for the various SWBLI cases in figure 1(*c*), the individual characteristics would all gradually change. However, specifically in the incident–reflected SWBLI case, a distinct threshold exists which marks the transition between a regular and an irregular reflection. As seen in figure 2(*a*), an inviscid regular reflection (RR) is characterised by an incident shock (*I*) impinging upon a wall which is simply reflected (*R*). In contrast, an inviscid irregular or Mach reflection (MR) is characterised by a more complex shock structure (figure 2*b*). The complicating feature in the irregular reflection is a near vertical third shock (*N*) which joins with *I* and *R* at a triple point at some distance from the reflecting surface, commonly referred to as a Mach stem. The flow characteristics of RR-SWBLI and MR-SWBLI can be drastically different. It is therefore very important to not only be able to accurately predict the point at which RR-SWBLI transitions to MR-SWBLI, but what factors may affect the transition.

https://doi.org/10.1017/jfm.2018.537 Published online by Cambridge University Press

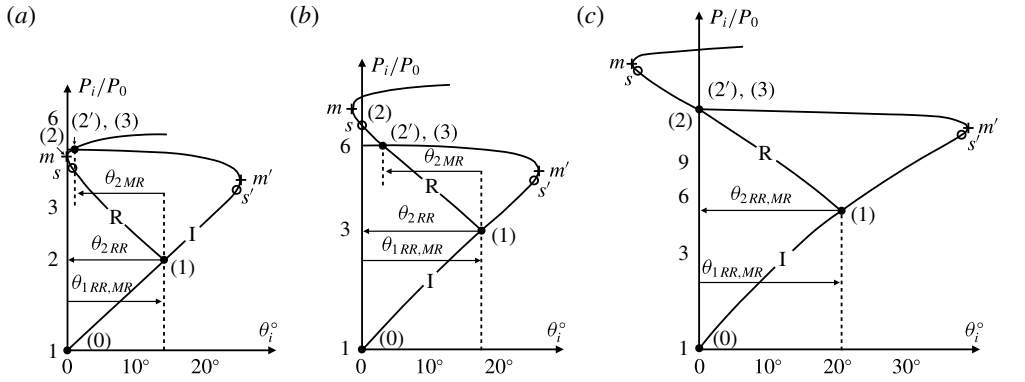

FIGURE 3. Shock polars demonstrating (*a*) the detachment criterion, (*b*) the sonic criterion and (*c*) the mechanical equilibrium criterion, adapted from Ben-Dor (2007).

1.1. *Inviscid transition criteria*

The core mechanism that requires a transition between RR and MR lies in the asymmetric parabolic relationship between the flow deflection (θ) and the oblique shock angle (β) for a given Mach number, as governed by the Rankine–Hugoniot relation. The inviscid flow conditions that result in either an RR or an MR as well as the transition between the two have been widely studied (Henderson 1967; Hornung, Oertel & Sandeman 1979; Hornung & Robinson 1982; Chpoun *et al.* 1995; Vuillon, Zeitoun & Ben-Dor 1995; Li & Ben-Dor 1997; Ben-Dor 2007).

These inviscid conditions are represented graphically in figure 3 by several pressure deflection diagrams or shock polars. In each plot, there are two polars, one for the incident shock (I) and one for the reflected shock (R). Three points are also annotated: (0), (1) and (2). These three points represent the flow states of the free stream, the region immediately downstream of the incident shock and the region immediately downstream of the reflected shock respectively.

The three accepted criteria for transition are the detachment criterion, the sonic criterion and the mechanical equilibrium (also known as the von Neumann) criterion. In all three plots, point (2) resides on the P_i/P_0 axis. In the case of the detachment criterion (figure 3*a*), any further increase in the incident shock strength through an increase in θ will cause the R polar to move to the right and shrink, detaching point (2) from the P_i/P_0 axis and jumping to the collocated (2′), (3), and the shock reflection will transition from RR to MR. The sonic criterion is very similar to the detachment criterion, but with the detachment point being the sonic point s instead of point m. The sonic criterion contends that prior to reaching point s, any downstream effects (such as the presence of an expansion fan) cannot affect the reflection as information can only propagate downstream; however, after exceeding point s, downstream information can propagate upstream to affect the reflection. Lock & Dewey (1989) demonstrated the sonic criterion through experiment, proving its validity, but found that it is mainly applicable to pseudo-steady flows. The mechanical equilibrium criterion, originally suggested by von Neumann (1943*a*,*b*) and studied in depth by Henderson & Lozzi (1975), provides for a smooth transition from RR to MR in that a section of polar R intersects the P_i/P_0 axis at the same point as the strong section of the I polar. This unique configuration of polars only exists for free-stream Mach numbers $M_0 \geqslant 2.2$, above which transitional hysteresis can occur, finding all

https://doi.org/10.1017/jfm.2018.537 Published online by Cambridge University Press

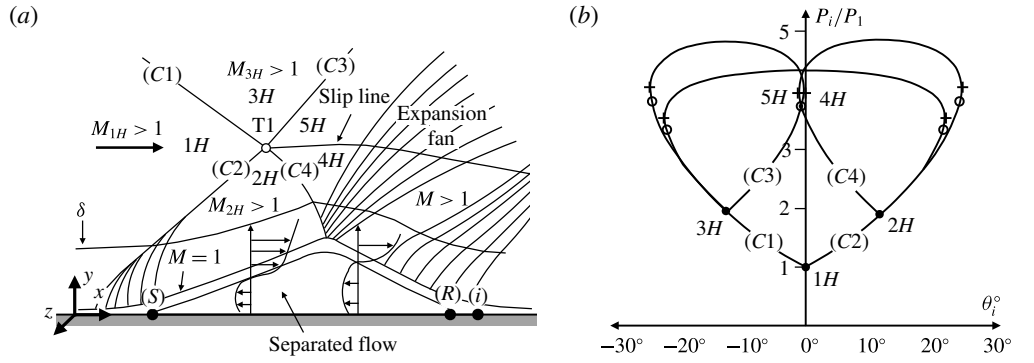

FIGURE 4. Moderate-strong SWBLI: (*a*) schematic diagram adapted and modified from Délery, Marvin & Reshotko (1986); (*b*) shock polar.

three criteria valid. However, for a steady flow with a free stream $1 \leqslant M_0 \leqslant 2.2$, only the detachment criterion is valid.

1.2. *The SWBLI transition*

Experimental investigation of transition criteria for inviscid shock reflections requires the removal of viscous effects such as the boundary layer at the reflecting surface. In practice, this is achieved through the creation of a symmetry plane in place of the wall, generated by an equal and opposite flow deflection with an equal and opposite oblique shock to generate an apparent RR or MR at the symmetry plane. However, the shock–shock interaction need not be perfectly symmetric, and transition can be observed with both symmetric and asymmetric interactions. In fact, Edney (1968) defined a classification system for such interactions, stating that there are six possible canonical shock–shock interaction types. Li, Chpoun & Ben-Dor (1999) investigated the reflection of asymmetric shock waves in steady flows for $M_0 = 4.96$, the results of which confirmed the detachment and mechanical equilibrium criteria as well as the dual solution domain which results in transitional hysteresis.

In the asymmetric study of Li *et al.* (1999), an opposing wedge is used to generate the opposing oblique shock. However, the use of a physical reflecting surface can also lead to an inviscid asymmetric shock–shock interaction, serving a similar purpose to the opposing wedge. An example of this can be seen in figure 4(*a*), which shows a schematic diagram of a strong separated SWBLI. In figure 4(*a*), the incident shock $C1$ is sufficiently strong to induce boundary layer separation between points S and R, and this separated region requires a flow deflection for the incoming supersonic flow, which gives rise to the separation shock $C2$, resulting in an inviscid asymmetric shock–shock interaction at point T_1. In this way, the separation region/bubble acts in a similar way to the opposing wedge in the asymmetric study of Li *et al.* (1999).

An accompanying example of an asymmetric shock polar for a strong SWBLI appears in figure 4(*b*). This shock polar, generated by an SWBLI, would be identical to an equivalent inviscid shock–shock interaction involving the same upstream flow conditions and flow deflection angles, analogous to those in the study of Li *et al.* (1999), and thus it becomes clear that SWBLIs can approximate asymmetric shock–shock interactions.

Very little research into transition in SWBLIs exist, although recently Matheis & Hickel (2015) numerically investigated an $M_0 = 2$ incident–reflected SWBLI

https://doi.org/10.1017/jfm.2018.537 Published online by Cambridge University Press

and transition between RR and MR. They performed three-dimensional large-eddy simulations (LES) without sidewalls with a spanwise domain of $L_z = 4\delta_{ref}$ and a Reynolds number of $Re_\delta = 4.8 \times 10^4$. They simulated a number of full-span shock generators with flow deflection angles of $\theta = 11°$, $12°$, $12.5°$, $13°$ and $14°$.

Matheis & Hickel (2015) found that transition occurred (in a time-averaged sense) at $\theta = 14°$. They obtained mean values of the flow deflection behind the separation shock (e.g. $C2$ in figure 4*a*) of $\theta' = 10.53°$, $11.41°$, $11.41°$, $11.41°$ and $11.50°$ for the $\theta = 11°$, $12°$, $12.5°$, $13°$ and $14°$ cases respectively. Based upon the obtained θ' values, Matheis & Hickel (2015) concluded that the time-averaged separation shock angle remains nearly constant when the flow deflection is $\theta > 11°$. Matheis & Hickel (2015) also contended that this behaviour is characteristic of the free interaction theory of Chapman, Kuehn & Larson (1958).

Matheis & Hickel (2015) pointed out, assuming that the flow downstream of the separation shock remains constant at $\theta' = 11.41°$, that the detachment criterion would predict transition to occur for an incident shock flow deflection of $\theta \geqslant 14.21°$, which is higher than what they observed. At $\theta = 11°$, they found the flow downstream of the SWBLI outside of the boundary layer to be fully supersonic. However, for $\theta \geqslant 12°$, they observed a small subsonic region immediately downstream of the SWBLI, centred around the shock interference triple point.

Matheis & Hickel (2015) chose to investigate $\theta = 13°$ without time-averaging to investigate unsteadiness in the SWBLI. They found that the instantaneous flow deflection downstream of the separation shock fluctuated in the range $10.08° < \theta < 12.88°$ and that the instantaneous flow deflection downstream of the incident shock fluctuated by of the order of $\pm 0.25°$. They contended that this combined fluctuation of incident and separation shock angles resulted in occurrences where the required maximum flow deflections of the incident and separation shocks were instantaneously exceeded. In these instances, Mach reflections were observed and the height of the Mach stem varied in time with an apparent dependence upon the extent to which the maximum flow deflections had been exceeded.

In general, such unsteadiness in shock-induced separation is a widely studied topic. It has been studied numerically by Touber & Sandham (2008, 2009, 2011), Agostini, Larcheveque & Dupont (2015) and experimentally/analytically by Ganapathisubramani, Clemens & Dolling (2009), Piponniau *et al.* (2009), Souverein, Bakker & Dupont (2013), Rabey & Bruce (2017) and Threadgill & Bruce (2017), to name just a few. However, the complete extent to which unsteadiness affects RR-SWBLI/MR-SWBLI transition, due to the limited number of studies regarding SWBLI transition, remains uncertain.

1.3. *Motivation*

As pointed out in the introduction, very little research into transition in SWBLIs exists. Matheis & Hickel (2015) investigated transition in SWBLI numerically, but to the best of the authors' knowledge there exists no such experimental study on the topic. Furthermore, Matheis & Hickel (2015) chose not to include the effect of sidewalls; however, it is widely known that the inclusion of sidewalls can have a large effect on the resulting flow (Bruce *et al.* 2011; Burton & Babinsky 2012; Babinsky *et al.* 2013; Benek, Suchyta III & Babinsky 2013; Galbraith *et al.* 2013; Wang *et al.* 2015). An experimental study would naturally include sidewall effects.

In addition to the above, in almost all experiments involving an oblique shock reflection, there exists a downstream expansion fan originating at the termination of

https://doi.org/10.1017/jfm.2018.537 Published online by Cambridge University Press

the oblique shock generating wedge. Matheis & Hickel (2015) stated that, in general, this expansion fan has a large effect on the stability of the resulting SWBLI, claiming that there is a direct relationship between the SWBLI–expansion-fan separation and the adverse pressure gradient seen at the point of reattachment by the separated shear layer. This raises the question of the relationship the downstream expansion fan has with the upstream SWBLI.

Furthermore, in studying transition in inviscid asymmetric shock–shock interactions, it is common to leave one flow deflection fixed and increase the other. The study of Matheis & Hickel (2015) closely represents such an attempt, inducing transition through increase in the strength of the incident oblique shock while assuming that the separation shock strength remains nearly constant. It should be recalled that Matheis & Hickel (2015) observed this to be the case and concluded that this behaviour was characteristic of the free interaction theory of Chapman *et al.* (1958). However, in light of their findings with respect to the triggering of transition, a question arises as to whether or not the time-averaged separation shock angle remains constant for all incident–reflected SWBLIs with separation and whether this is characteristic of free interaction theory.

Lastly, it should be mentioned that unsteadiness in shock-induced separation probably plays a large role in triggering transition between RR-SWBLI and MR-SWBLI, as Matheis & Hickel (2015) concluded. However, due to the low number of studies on the topic of SWBLI transition, basic questions remain regarding the general quasi-steady state arrangement and characteristics of SWBLI during transition.

In this study, we present the results from experiments with a novel set-up that allows us to (1) experimentally observe transition of an incident–reflected SWBLI, (2) explore the relationship between the proximity of the downstream expansion fan and the SWBLI, and (3) investigate the applicability of free interaction theory in defining the mean separation shock angle. The experimental set-up, namely the wind tunnel facility, the traversable oblique shock generator and the experimental techniques used, are described in § 2. Results are presented and discussed in § 3, showing transition from RR to MR without an increase in incident shock strength as well as a relationship between separation bubble size, separation shock strength and expansion fan proximity. The key conclusions of the study are summarised in § 4 along with suggestions for future work.

2. Methodology

2.1. *Wind tunnel*

This investigation was conducted in the Imperial College London supersonic wind tunnel facility. A schematic diagram of the tunnel test section appears in figure 5. The Mach 2 blow-down wind tunnel is supplied with dried air stored in four 12 m^3 tanks pressurised to 2.7 MPa and exhausts to atmosphere. The test section has dimensions of 150 mm wide $\times$ 150 mm tall $\times$ 727 mm long and a unit Reynolds number of approximately 2.0×10^7 m^{-1}. The desired flow conditions are achieved through the use of a PID controlled pneumatic pressure valve that maintains a commanded ratio of stagnation to atmospheric pressure (typically 1.8–2.9). Downstream of the control valve, turbulence levels are reduced by passing the flow through a settling chamber containing mesh screens and honeycomb prior to entering the nozzle and test section.

The test section boundary layer was characterised through the use of laser Doppler anemometry at a location immediately upstream of the SWBLI. The results are

https://doi.org/10.1017/jfm.2018.537 Published online by Cambridge University Press

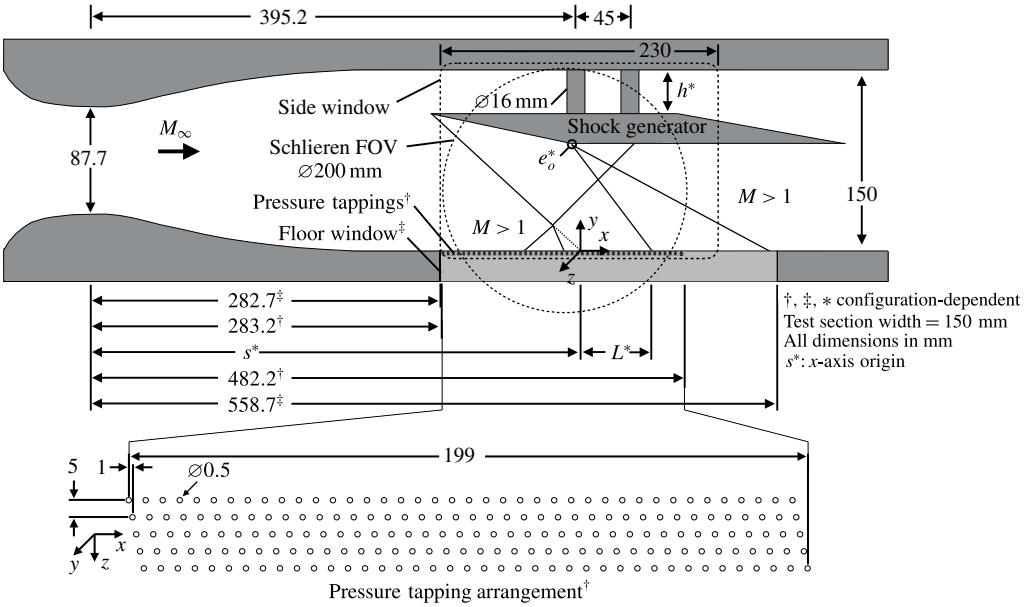

FIGURE 5. Schematic diagram of the wind tunnel set-up (see table 3 for the variable parameters s, h, L and e_o).

(x, z) (mm)	M_0	δ (mm)	δ_i^* (mm)	θ_i (mm)	H_i	Re_{θ_i}	C_f	u_τ (m s^{-1})
$(-75.4,\ 0)$	2	5.33	0.64 (1.20†)	0.50 (0.41†)	1.27	12483 (10124†)	0.0025	19.02

TABLE 1. Incompressible boundary layer profile parameters at streamwise locations (x, z) based upon an $h = 0$, 12° shock generator configuration. A dagger indicates a compressible value.

reported in table 1 for boundary layer thickness (δ), displacement thickness (δ_i^*), momentum thickness (θ_i), shape factor (H_i), Reynolds number (Re_{θ_i}), coefficient of friction (C_f) and friction velocity (u_τ).

The general test configuration in figure 5 features a shock generator suspended at some distance from the wall (h) which, during wind tunnel operation, generates an oblique shock wave originating from the tip. The shock wave impinges upon the wind tunnel floor boundary layer, resulting in an SWBLI. The inviscid impingement point at a distance s from the nozzle throat marks the origin of the coordinate system for each test case. An expansion fan also originates from the corner (e_o) on the underside of the shock generator. The relative arrangement of these features is dependent upon both the shock generator geometry and its deployed position h, and is discussed in the following section. The z-axis origin is the test section centreline.

2.2. *Shock generators*

Four different oblique shock generator geometries were used. All were made of steel and took the form of three-dimensional parallelograms with a 12° upstream facing wedge angle and 10° downstream facing wedge angle. Care was taken to machine

https://doi.org/10.1017/jfm.2018.537 Published online by Cambridge University Press

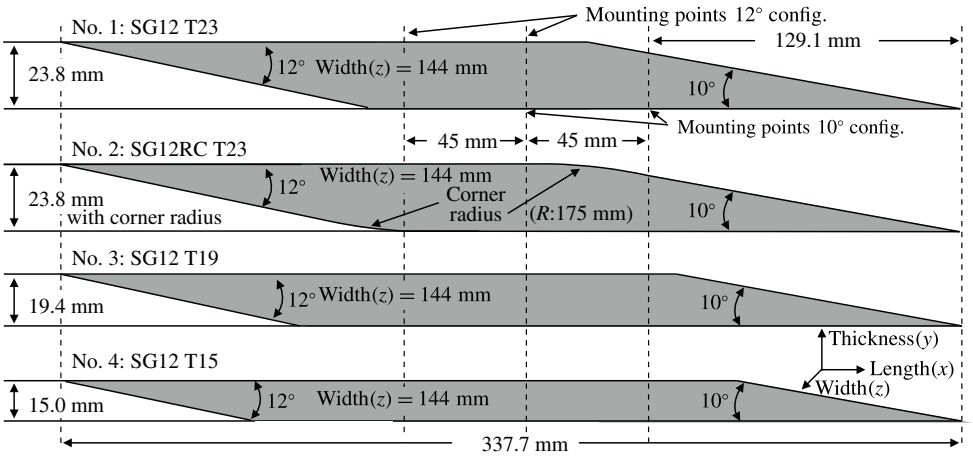

FIGURE 6. Shock generator schematic diagrams.

Shock generator	θ_{nom} (deg.)	U θ_{meas} (deg.)	D θ_{meas} (deg.)
No. 1: SG12T23	12	12.05	10.11
No. 2: SG12RCT23	12	12.01	10.07
No. 3: SG12T19	12	12.05	10.05
No. 4: SG12T15	12	12.05	10.04

TABLE 2. Nominal and measured test article upstream (U) and downstream (D) facing wedge angles.

the wedge angles to a high tolerance, as confirmed by the accurate post-machining measurements listed in table 2. The shock generators were mounted to two struts which straddled the point of zero aerodynamic moment for each configuration. These struts protruded through access holes in the tunnel ceiling supported by two large linear bearings and attached to a traverse which allowed fine stream-normal adjustment of the tip of the shock generator in the y-axis of $t < y < 150$ mm (dependent upon shock generator thickness t). The dimensions of the four shock generators are illustrated in figure 6. The shock generator label specifies the integer values for flow deflection angle in degrees plus any modifiers such as a rounded corner (e.g. SG12RC), and thickness in mm (e.g. T23).

All of the shock generators were 337.7 mm long and 144 mm wide (96 % span) giving 3 mm sidewall gaps to allow vertical traversing during wind tunnel operation. They were all identical except for the thickness (t) of the shock generator (T), which for nos. 1, 3 and 4 was set to 23.8 mm, 19.4 mm and 15.0 mm respectively. Shock generator no. 2 was identical to no.1 except for a 175 mm radius cut into the expansion fan sharp corner. By varying the thickness of the shock generator, the placement of the expansion fan origin e_o is physically shifted. By putting a radius on the expansion fan corner, e_o is virtually shifted upstream and stream-normal relative to the non-radius case of the same thickness, with the virtual e_o being defined as the origin of a virtual expansion fan possessing the same first and last expansion fan characteristic impingement points as the actual expansion fan resulting from a rounded corner.

https://doi.org/10.1017/jfm.2018.537 Published online by Cambridge University Press

Shock Gen.	AR_{eff}	h (mm)	s (mm)	x_{e_o} (mm)	y_{e_o} (mm)	L (mm)
No. 1: SG12T23	1.00	0.0	439.7	−51.2	126.2	45.3
No. 1: SG12T23	1.35	38.9	397.4	−8.9	87.3	57.9
No. 2: SG12RCT23	1.00	0.0	439.7	−81.6	154.5	36.5
No. 2: SG12RCT23	1.25	30.0	407.1	−49.0	124.5	46.2
No. 2: SG12RCT23	1.35	38.9	397.4	−39.3	115.6	49.1
No. 3: SG12T19	1.00	0.0	439.7	−71.9	130.6	28.0
No. 3: SG12T19	1.35	38.9	397.4	−29.6	91.7	40.6
No. 4: SG12T15	1.00	0.0	439.7	−92.6	135.0	10.7
No. 4: SG12T15	1.25	30.0	407.1	−59.9	105.0	20.3
No. 4: SG12T15	1.35	38.9	397.4	−50.3	96.1	23.2

TABLE 3. Key dimensions of expansion fan origin placement and separation for all configurations tested (reference figure 5).

Use of a traverse to adjust stream-normal placement (h) of the upstream leading edge of the shock generator allows an effective change in the wind tunnel aspect ratio and confinement. We define this effective change in aspect ratio (AR_{eff}) as the test section width divided by the height of the shock generator upstream leading edge. This yields a trend of an increase in AR_{eff} and a greater confinement or area reduction as the shock generator is lowered. An AR_{eff} range of 1.00–1.38 was found to be achievable for all configurations. A change in AR_{eff} also has an effect on the placement of e_o (x_{e_o}, y_{e_o}) relative to the inviscid incident oblique shock impingement point. This results in various distances L (see figure 5) between the inviscid incident oblique shock impingement and expansion fan impingement. These values are listed in table 3 and represent all of the test cases considered.

2.3. *Experimental techniques*

The flow fields produced in this study were observed utilising a combination of measurement techniques including Schlieren photography, particle image velocimetry (PIV), surface oil flow visualisation and high-spatial-resolution static pressure tappings.

Schlieren photography allowed the visualisation of detailed SWBLI shock structures as well as larger field of view items such as the incident oblique shock, reflected shock and expansion fan. A 'Z' configuration was used consisting of an LED point light source with 1 mm pin hole filter projecting onto a 200 mm diameter hemispheric mirror with a 1200 mm focal length. A second hemispherical mirror focused the light down to a conventional vertical oriented 'knife-edge' and was passed through a 105 mm lens (Sigma EX DG Macro) with an f-stop of 2.8. The resulting image was recorded with a high-speed camera (Phantom v641). The high-speed camera recorded 300 frames a second at a resolution of 2048×1536 ($\approx$8.6 pix mm^{-1}) with an exposure of 30 μs.

Planar vector fields were obtained through the use of PIV. Illumination was provided by a Nd:YLF class IV laser outputting 30 mJ pulse^{-1} at a wavelength of 527 nm. The laser beam was formed into a 2 mm thick sheet with beam to sheet forming optics. Di-ethyl-hexyl-sebacat droplets, of approximately 0.3 μm mean diameter, were injected into the settling chamber of the tunnel ahead of the flow conditioning screens from six radially spaced probes connected to an aerosol pumping system (PivTec).

https://doi.org/10.1017/jfm.2018.537 Published online by Cambridge University Press

Field of view	104.27 × 65.24 mm
Digital image resolution	24.6 pixels mm^{-1}
Interrogation window	32 × 32 and 16 × 16 pixels
f-stop and focal length	N/A*
Δt	1.4 μs
Particle diameter	0.3 μm
Window overlap	75 %
Vector spacing	0.33 × 0.33 mm
Telecentric lens magnification	0.245

TABLE 4. The PIV measurement parameters. *Note: telecentric lenses have no practical focal length or f-stop.

For each configuration, 2732 image pairs were captured from a single high-speed camera (Phantom v641), at 720 Hz, attached to a telecentric lens (Opto Engineering TC16M-144) at a distance of approximately 400 mm from the interaction. The exact parameters used in this investigation can be found in table 4. Unlike the schlieren photography, the PIV results were obtained in individual runs of the wind tunnel due to data acquisition limitations, and therefore a small velocity correction (relative to the first experiment) was necessary to account for slight variations in temperature between runs.

Surface oil flow visualisation was achieved by injecting a high-contrast oil mixture over a matte black floor plate just upstream of each SWBLI. The mixture consisted of titanium dioxide, oleic acid and kerosene, and was filmed through a sidewall window using a camera (Nikon D7000 DSLR) in video mode. Schematics of the imaged surface oil flow topologies were generated by tracing over the streamlines present in the images. All images presented in this study were imaged *in situ* during the experiment to avoid any wind tunnel shut down transient and/or erroneous features that could be imprinted after the fact. During each wind tunnel experiment, a still frame was selected from the video and dewarped with the aid of a calibration target (imaged before each experiment) to correct for camera perspective and to provide physical scale.

Streamwise high-spatial-resolution (1 mm) static pressure measurements were obtained through the resulting SWBLIs. Geometrical constraints precluded the static pressure tappings from being aligned perfectly on the centreline. Instead, 1 mm streamwise precision was achieved with a staggered array of 200 static pressure ports, the arrangement of which is illustrated in figure 5. Two 16-channel pressure transducer arrays (Pressure Systems 9116 Netscanner) were used. Collection of data across the 199 mm range required the wind tunnel to be repeatedly run for an identical configuration, disconnecting previously measured static tappings and reconnecting new static tappings (all disconnected tubes were fitted with plugs to ensure no leakage of flow from outside the test section). The pressure transducers were recalibrated before every measurement to null offset drift errors, as well as wind tunnel runs being performed in quick succession to avoid any drift due to changes in the atmospheric conditions. The use of this procedure resulted in composite pressure profiles that fell well within the measurement accuracy of the pressure transducers (±0.0135 psia).

https://doi.org/10.1017/jfm.2018.537 Published online by Cambridge University Press

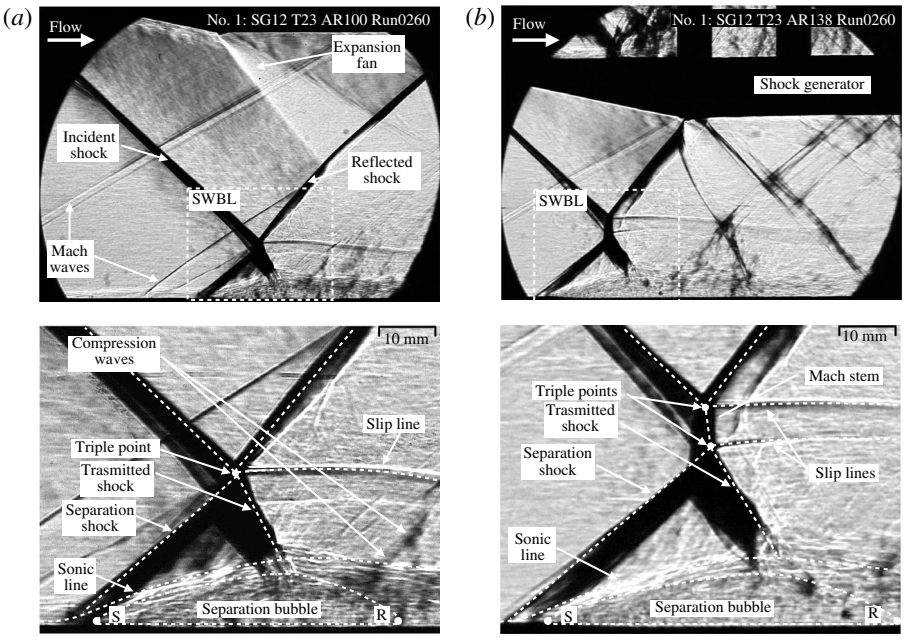

FIGURE 7. Schlieren photography of no. 1: SG12T23 SWBLI showing the effect of $AR_{eff} = 1.00$–1.38 ($M_0 = 2$, $\theta = 12°$): (*a*) $AR_{eff} = 1.00$; (*b*) $AR_{eff} = 1.38$.

3. Results

3.1. *Regular–irregular transition*

In this section, results obtained with the no. 1: SG12T23 shock generator at AR_{eff} in the range 1–1.38 are presented. The evolution of the SWBLI structure is shown through schlieren photography.

The $\theta = 12°$ flow deflection yields a strong SWBLI which results in both a large well-defined SWBLI structure and a large region of shock-induced boundary layer separation. Figure 7 shows the large-scale field of view of the interactions along with detailed views for the $AR_{eff} = 1.00$ and $AR_{eff} = 1.38$ cases. The images in figure 7 were all taken from a single wind tunnel run separated by approximately 15 s with all conditions held constant except AR_{eff}. In the images, several features can be seen: the shock generator, the incident shock, the reflected shock, an expansion fan, the SWBLIs themselves and a few Mach waves originating from wall joints or imperfectly cancelled waves from the nozzle expansion which are so weak that they do not influence the flow. In both cases, the adverse pressure gradient imposed by the incident oblique shock causes the boundary layer to separate. The approximate extent of flow separation is marked by S and R and enclosed by a dotted line in both figures, as indicated by the separation shock and compression waves respectively. The flow is deflected up away from the wall and over the separation bubble by the separation shock, before being turned back down as it travels through the transmitted shock. The separation shock travels up and interacts with the original incident shock. The SWBLI seen in figure 7(*a*), using the classification system of Edney (1968) mentioned in the introduction, would be regarded as a type I interference, which corresponds to an RR-SWBLI. In the figure, from the point of interference or triple point, two other shocks emanate away. One is the reflection from the incident shock (travelling

https://doi.org/10.1017/jfm.2018.537 Published online by Cambridge University Press

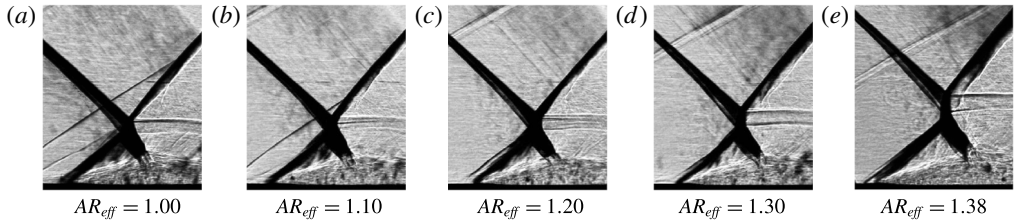

FIGURE 8. The SWBLI structure evolution for no. 1: SG12T23, $AR_{eff} = 1.00$–1.38.

away from the floor) and the other is commonly referred to as the 'transmitted' shock (travelling towards the floor). These two shocks turn the two flows above and below the triple point back parallel to each other. Also originating at the triple point and travelling downstream is a slip line. The presence of a slip line is indicative of an entropy mismatch between the paths above and below the triple point as they encounter shocks of different strengths. Downstream of the SWBLI, the expansion fan impinges upon the floor. The role of the expansion fan in affecting the SWBLI will be discussed later in § 3.4.

Figure 7(*a*) shows a broadly similar SWBLI structure to that in figure 7(*b*). However, in 7(*b*), the SWBLI features two slip lines and two triple points, with a near-normal shock region joining the triple points together. This structure is classified by Edney (1968) as a type II interference, corresponding to a Mach reflection (MR) SWBLI. At this higher AR_{eff}, the separation bubble is larger (as indicated by larger streamwise displacement of the separation and transmitted shock), and the presence of an MR-SWBLI suggests that the flow must be turned by a greater amount. As the flow is deflected up away from the wall and over the separation bubble, it must again be turned back down as it travels through the transmitted shock. The presence of a type II interference suggests that the flow turning angle required to turn the flow parallel to the incoming flow as it passes through the transmitted shock is in excess of the maximum turning angle for the flow (θ_{max}) as defined by the solution to the Rankine–Hugoniot equations (θ–β–M relationship). In this situation, the flows above and below the triple points can no longer be turned parallel to each other. This is evident in the way that the slip lines are very slightly angled towards each other with a narrowing distance between them as they flow downstream. In order to satisfy these flow conditions, a near-normal shock or Mach stem forms between the two triple points, with the region immediately behind the Mach stem being subsonic. Further downstream, the narrowing of slip lines causes reacceleration of the post-shock flow, eventually returning to supersonic speeds. The evolution of the SWBLI with changing AR_{eff} is studied in more detail in figure 8, which shows the gradual transition of the SWBLI from RR to MR at intermediate values of AR_{eff}. In the figure, the SWBLI size is seen to increase with an increase in AR_{eff}. Here, we define SWBLI size as the height of the triple point(s) above the wind tunnel floor.

3.2. *Change in boundary layer parameters with effective aspect ratio*

Specific to the arrangement used in the current study, boundary layer parameters do vary slightly for SWBLIs at different values of AR_{eff} due to the fact that as AR_{eff} is increased, the shock impingement point moves upstream relative to the shock generator and therefore experiences a boundary layer at a different stage of development. This movement spans $\Delta x \approx 46$ mm ($\approx 8.6\delta$) for $AR_{eff} = 1.00$–1.38. In the

https://doi.org/10.1017/jfm.2018.537 Published online by Cambridge University Press

previous section, it was seen that an increase in AR_{eff} is accompanied by an increase in SWBLI size and strength. Since the boundary layer parameters are different for each case presented in figures 7 and 8, the question of boundary layer influence on the observations needs to be addressed.

A study by Threadgill & Bruce (2016) was performed in the same wind tunnel at the same free-stream conditions. In the study, the evolution of the boundary layer profile was characterised from ≈95 to 45 mm upstream of the $AR_{eff} = 1.00$ inviscid shock impingement point. Across this distance, δ grew by ≈0.2 %/mm. However, the shape factor (a parameter that has a large effect on SWBLI structure) remained nearly constant. Furthermore, not only is the expected change in boundary layer thickness over this distance small, but the trend is such that as AR_{eff} is increased, the SWBLI will experience a smaller boundary layer thicknesses. With this trend, one might expect to see a trend of smaller SWBLIs at higher values of AR_{eff}. However, as shown in figures 7 and 8, the effect of AR_{eff} is so strong that it overcomes this boundary layer effect and the growth of SWBLIs at higher values of AR_{eff} is observed.

3.3. *Average centreline velocity field and separation topology*

Although the images in figures 7 and 8 are representative of the flow field for each test case, some unsteadiness of the flow was observed and hence frame-to-frame variations. Therefore, in order to infer the shock angles, particularly for the separation shock, mean velocity field measurements (averaged over 3.8 s) were obtained with PIV. In figure 9, the PIV velocity fields around the $\theta = 12^\circ$ SWBLI are presented. Figure 9(*a*,*c*,*e*) shows the SWBLI when AR_{eff} is set to 1.00 and figure 9(*b*,*d*,*f*) shows the SWBLI when AR_{eff} is set to 1.38.

When the AR_{eff} is increased from 1.00 to 1.38, the evolution from RR-SWBLI (figure 9*a*) into MR-SWBLI (figure 9*b*) can again be observed. In figure 9(*b*), the region at approximately $x \approx -25$ mm, $y \approx 30$ mm qualitatively grows in size and the formation of the Mach stem is seen as the interaction/triple point between the incident and reflected shocks moves up away from the interaction/triple point of the separation and transmitted shock. The root mean square (RMS) plot in figure 9(*d*) shows the result quite clearly. Looking at the PIV results qualitatively, the onset of MR-SWBLI causes the single slip line seen in figure 9(*c*) to pull apart into two slip lines in figure 9(*d*) that persist downstream for the extent of the field of view.

Figure 9(*e*,*f*) shows the evolution of the stream-normal velocity contours with increasing AR_{eff}. Comparing the region in the vicinity of the slip line(s) for $AR_{eff} = 1.00$ and 1.38, a condition is observed that agrees with the MR-SWBLI. When the RR-SWBLI is present, it can be seen that there exists a larger region of zero stream-normal velocity (white) behind the reflected shock, and that both the upward travelling flow (green) behind the transmitted shock and the downward travelling flow (blue) behind the reflected shock are more confined, which is consistent with an RR-SWBLI, i.e. the disparity between flow above and below the triple point is smaller and the flows can achieve equilibrium with one slip line. When the MR-SWBLI is present, the opposite occurs, with the upward travelling and downward travelling flow regions growing in size, consistent with a disparity between flows that cannot reach equilibrium and requires the formation of the Mach stem with two slip lines.

The above described evolution can be explored further by plotting shock polars for the incident and separation shocks for each interaction, based upon shock angles measured from PIV with an uncertainty of better than $\pm 0.1^\circ$. Figure 10(*a*) represents

https://doi.org/10.1017/jfm.2018.537 Published online by Cambridge University Press

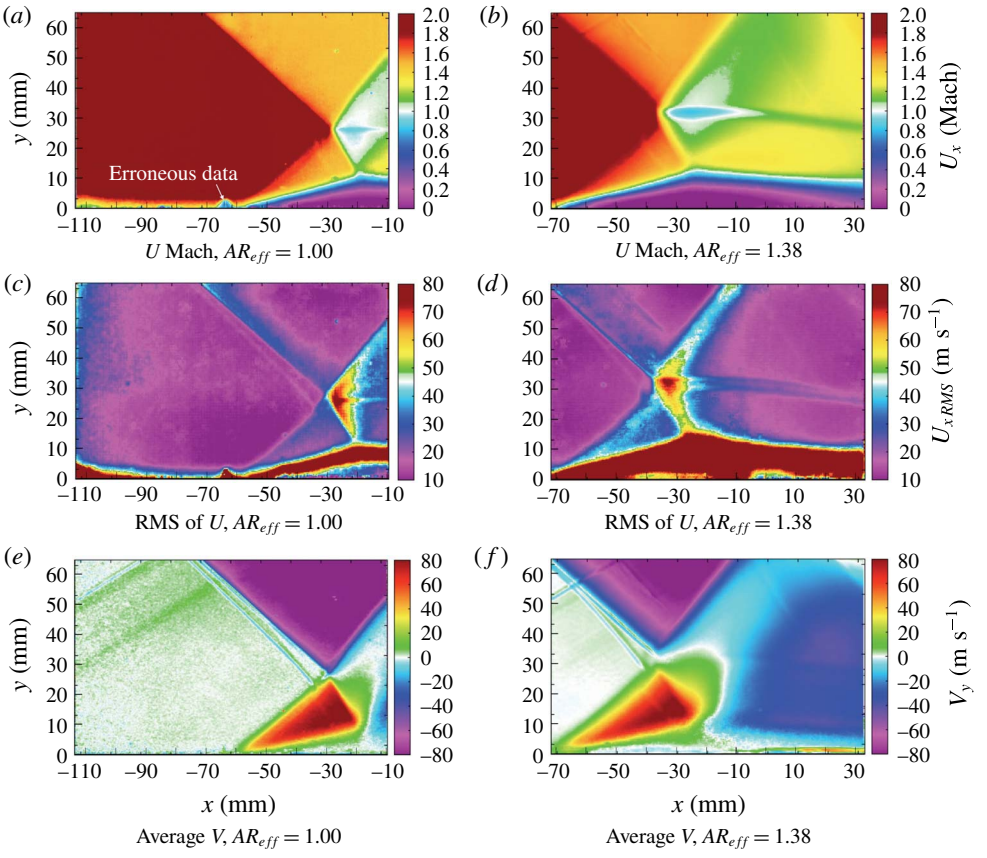

FIGURE 9. (Colour online) The PIV velocity field measurements for no. 1: SG12T23 SWBLI, $AR_{eff} = 1.00$–1.38 ($M_0 = 2$, $\theta = 12°$).

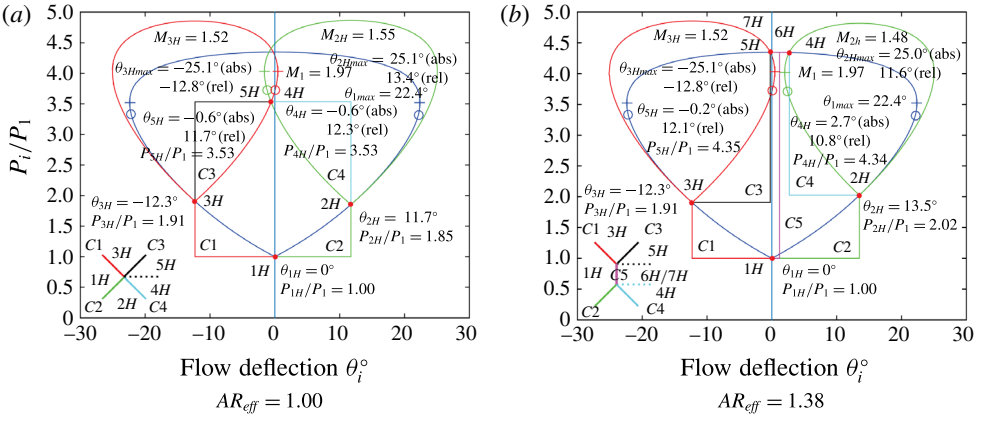

FIGURE 10. (Colour online) Effect of AR_{eff} on shock polar plots for SWBLIs with $\theta = 12°$.

the $M_0 = 2$, $\theta = 12°$ SWBLI at $AR_{eff} = 1.00$, with figure 10(*b*) representing the equivalent SWBLI at $AR_{eff} = 1.38$. The legend at the bottom left of figure 10(*a*) is different from that in 10(*b*), representing the addition of the Mach stem shock *C*5.

https://doi.org/10.1017/jfm.2018.537 Published online by Cambridge University Press

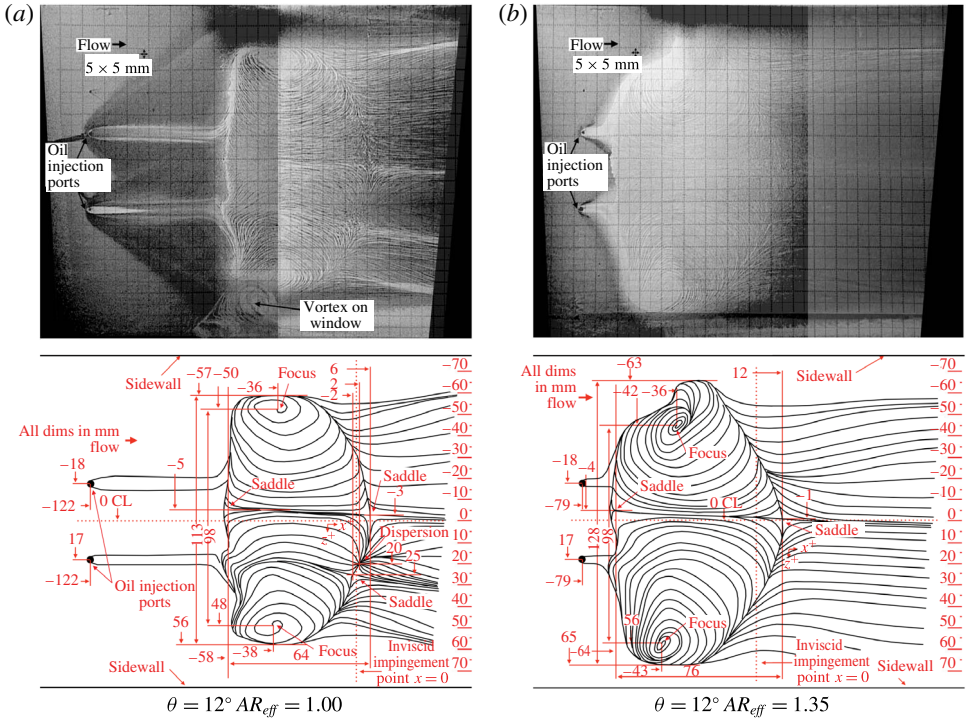

FIGURE 11. (Colour online) Flow separation region topology for no. 1: SG12T23, AR_{eff} = 1.00–1.35.

As AR_{eff} increases, the angle of the incident shock is unchanged while the angle of the separation shock (β_{C2}) is observed to increase from 41.9° to 44.1°, corresponding to deflections of $\theta_{2H} = 11.7°$ to 13.5° respectively. With the increase in β_{C2}, the path $C2$ and state $2H$ rise further up the $1H$ shock polar, resulting in a decrease in the size of the subsequent shock polar originating at point $2H$. The shock polars illustrate how points $2H$ and $3H$ can no longer achieve a collocated $5H$ and $4H$ state: state $4H$ is beyond the θ_{max} of state $3H$ and likewise state $5H$ is beyond the θ_{max} of state $2H$. With the separation of states $5H$ and $4H$, the creation of the Mach stem (i.e. a very slightly curved shock $C5$) to satisfy this state mismatch is seen. The appearance of shock $C5$ also reveals a new path from state $1H$ to later states. The flow can now jump directly to the new states $7H$ and $6H$. States $7H$ and $5H$ reach adjacent locations along different paths and again require a slip line border between them separating the different entropy states, and likewise for states $6H$ and $4H$. Thus, figure 10 confirms that the observed shock angles are consistent with the transition behaviour.

Figure 11 shows the effect of AR_{eff} on the topology of the separated region on the wind tunnel floor, as seen through the use of surface oil flow visualisation. Images for $AR_{eff} = 1.00$ and 1.35 are shown in figures 11(a) and 11(b) respectively. It should be noted that $AR_{eff} = 1.35$ was used instead of 1.38 due to the fact that the initial injection of oil causes a temporary flow disturbance, and a reduction in AR_{eff} is required to avoid wind tunnel un-start.

Inspection of figure 11(a) ($AR_{eff} = 1.00$) reveals many notable features. Most apparent is the large region of reversed flow, bounded by the upstream accumulation of oil mixture in a largely stream-normal direction and the downstream concave line of

https://doi.org/10.1017/jfm.2018.537 Published online by Cambridge University Press

streamline branching. With the theoretical inviscid impingement point of the incident shock marking the $x = 0$ axis and the tunnel centreline marking the $z = 0$ axis, the area is bounded by $-58 < x < 6$ mm and $-57 < z < 56$ mm. Within this region, there exist six critical points: two focus points, three saddle points and one dispersion node. The arrangement of these points and the general topography is similar to the 'owl-face' separated flow pattern described by Perry & Chong (1987). The stream-normal width of the separated region as measured from the outer edges of these vortices is 113 mm. Two saddle points exist at $(x, z) = (6, -3)$ mm and $(x, z) = (-2, 25)$ mm and a third at approximately $(x, z) = (-58, -5)$ mm. The locations of these saddle points demonstrate that there is a small amount of asymmetry in the separation topology, in that one would expect them to be evenly distributed about the centreline ($z = 0$ mm). In between the two downstream saddle points is a dispersion node, i.e. a node with streamlines flowing away located at $(x, z) = (2, 20)$ mm. The shock-induced separation begins at a roughly stream-normal lateral line along $x = -58$ mm. Flow reattachment occurs along the curved line that begins and ends tangent to the outer edges of the two vortices (i.e. $(x, z) = (-36, -57)$ mm and $(x, z) = (-38, 56)$ mm). The apex of this curve, which represents the furthest downstream reattachment point, is actually the saddle point located at $(x, z) = (6, -3)$ mm, yielding a centreline streamwise separation length of 64 mm.

It should be noted that the desire to accurately represent the extent of the separated region in this study has led to a definition of a 'centreline separation length' that both may not be the largest streamwise length present and may not exist exactly on the wind tunnel centreline. The definition used in this study is the distance between the apex of the curved reattachment line (which is typically close to the wind tunnel centreline) and an average separation line (mostly straight in a lateral direction). It is believed that this definition gives the best insight into the size of the separated region and very closely correlates with SWBLI size.

Figure 11(*b*) ($AR_{eff} = 1.35$) shows many of the same features as figure 11(*a*). However, the centreline streamwise length of the separation region has grown considerably to 76 mm (≈19 %). This growth in separation length is in agreement with the observations made with the schlieren photography and PIV, namely that the size of the interaction and hence the length of the separation bubble grows with increasing AR_{eff}. Furthermore, the total number of critical points has been reduced to four, with the disappearance of one saddle point and the dispersion node along the reattachment line. The remaining saddle point on the reattachment line has moved now almost directly onto the tunnel centreline. The two counter-rotating vortices remain the same distance apart, but are skewed towards one side of the wind tunnel. A bulge in the topology pattern, at approximately $(x, z) = (-30, -63)$ mm, appears to have pushed the vortex at $(x, z) = (-36, -42)$ mm towards centreline. However, the root cause for this lateral shift is unknown.

3.4. *The role of the expansion fan*

In the preceding sections, it was seen how an increase in AR_{eff} resulted in transition between RR-SWBLI and MR-SWBLI without requiring an increase in incident shock strength. As AR_{eff} is increased for the configuration in this study, the relative orientation of the SWBLI and the expansion fan emanating from the underside of the shock generator is altered. To examine the effect of expansion fan proximity on the SWBLI, we investigate the mechanisms that can affect it. The placement of the expansion fan can be affected not only through a change in AR_{eff}, but it can be

https://doi.org/10.1017/jfm.2018.537 Published online by Cambridge University Press

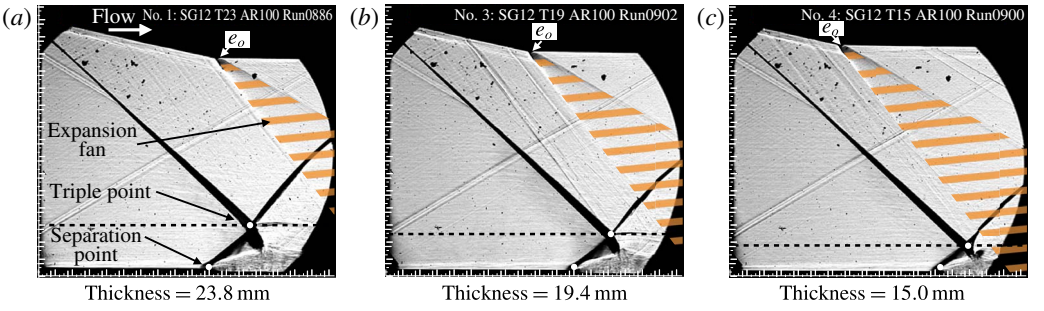

FIGURE 12. (Colour online) Schlieren photographs showing the effect of expansion fan placement on incident–reflected SWBLIs for (*a*) no. 1: SG12T23, (*b*) no. 3: SG12T19 and (*c*) no. 4: SG12T15 ($M_0 = 2$, $\theta = 12°$, $AR_{eff} = 1.00$).

physically and virtually shifted as well by varying the shock generator thickness and the rounding of the expansion fan corner respectively.

Figure 12 shows the effect of varying the shock generator thickness on the SWBLI. The test configurations in figure 12 are identical in every way except for the shock generator thickness (i.e. identical flow deflection angles, identical inviscid incident shock impingement points and identical inflow boundary layer parameters). As the shock generator thickness is reduced from 23.8 mm to 19.4 mm and then to 15.0 mm, the expansion fan origin location changes from $e_0 = (-51.2, 126.2)$ to $(-71.9, 130.6)$ to $(-92.6, 135.0)$ respectively. This results in a progressive shift upstream and stream-normal (away from the wind tunnel floor) in each case of $\Delta x = -20.7$, $\Delta y = 4.4$ mm, with the overall effect of bringing the expansion fan first characteristic and impingement point closer to the SWBLI. The result of this is that the overall size of the SWBLI is observed to reduce as the expansion fan is moved closer to the SWBLI. The case presented in figure 12(*a*) is the same as that presented in figure 7(*a*), which represented an RR and thus was classified as an Edney type I interference (RR-SWBLI). As the expansion fan is moved forward in figure 12(*b*,*c*), the triple point can be seen to reduce in height above the wind tunnel floor. However, there is no change in the general organisation of the SWBLI structure. As such, the classification of RR-SWBLI remains the same for all three SWBLIs. Apparent in the figure and in agreement with the reduction in size of the SWBLI, the separation point noticeably moves downstream as the expansion fan origin is moved upstream, which is indicative of a decrease in the streamwise extent of the separated region.

Photographs of the separated region topology with accompanying streamline schematic diagrams for all three cases can be seen in figure 13. All three cases feature boundary layer separation, although the overall size of the separated region is reduced as the expansion fan is moved upstream. The primary indication of this is the streamwise separation length, which is reduced from 64 to 49 to 38 mm. Figure 13(*a*) is the same as figure 11(*a*), which featured six critical points: two focus points, three saddle points and one dispersion node. As the expansion fan is moved upstream in the other two cases (figure 13*b*,*c*), all six critical points persist, although their relative positions vary. The movement of the critical points is associated with an increase in the overall asymmetry of the separated region (either side of centreline). With the initial change in thickness from 23.8 mm to 19.4 mm, the saddle point along the separation line at $(x, z) = (-58, -5)$ mm in figure 13(*a*) appears in an entirely different place, moving 23 mm to the other side of the centreline at $(x, z) = (-45, 18)$ mm in

https://doi.org/10.1017/jfm.2018.537 Published online by Cambridge University Press

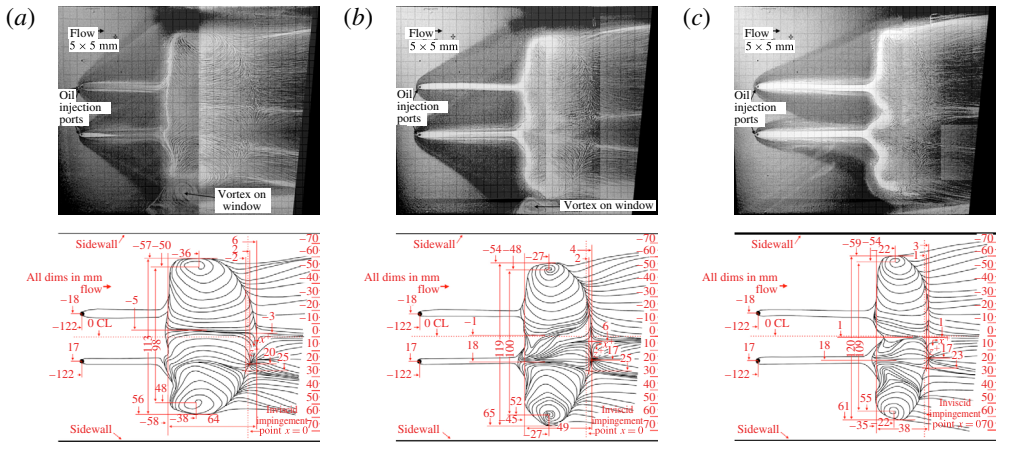

FIGURE 13. (Colour online) Flow separation topology showing the effect of expansion fan placement on (*a*) no. 1: SG12T23 (thickness = 23.8 mm), (*b*) no. 3: SG12T19 (thickness = 19.4 mm) and (*c*) no. 4: SG12T15 (thickness = 15.0 mm) ($M_0 = 2$, $\theta = 12°$, $AR_{eff} = 1.00$; not to scale with figure 12).

figure 13(*b*). This movement of the separation saddle point has a large effect on the streamlines in the centre of the separated region, disrupting their path and drawing in those in close proximity to the saddle point. The saddle points and dispersion node along the reattachment line maintain their local arrangement, although the saddle point originally located at $(x, z) = (6, -3)$ mm in figure 13(*a*) has also moved to the other side of the centreline in figure 13(*b*), though to a lesser degree than the movement of the saddle point on the separation line. The counter-rotating vortices originally centred at $(x, z) = (-36, -50)$ mm and $(x, z) = (-38, 48)$ mm in figure 13(*a*) have shifted slightly further apart (from 98 to 100 mm) in figure 13(*b*), and the distance between the vortex centre and the outer edge has increased, resulting in a larger separation width (from 113 to 119 mm).

When the expansion fan is moved still further upstream, as is the case in figure 13(*c*), the separated region topology remains largely the same as in the previous case (figure 13*b*). However, the separation length decreases further and the side vortices shift 9 mm further apart, although this shift is accommodated without a significant change in the overall width of the separated region (119 versus 120 mm). The saddle point along the separation line remains in the same location in figure 13(*c*) as in figure 13(*b*), although the disturbance caused to the adjacent streamlines has increased, most notably with a dent in the separation line around $z = 1$ mm and to a lesser extent at $z = 35$ mm in figure 13(*c*). This arrangement is indicative of an overall weaker separated region that may be on the verge of necking down at these points and forming distinct separation cells.

Figures 14 and 15 show the impact that rounding the corner on the 23.8 mm thick shock generator has on the expansion fan placement. As with a change in shock generator thickness, both figures 14(*a*) and 14(*b*) have identical flow deflection angles, inviscid impingement points and inflow boundary layer parameters.

Relative to the expansion fan origin (e_0) in figure 14(*a*), the corner rounding has virtually shifted e_0 by $\Delta x \approx -31$ mm, $\Delta y \approx 28$ mm in figure 14(*b*), which results in an upstream shift in the expansion fan first characteristic impingement. This upstream movement yields a result that is qualitatively similar to those seen in figures 12

https://doi.org/10.1017/jfm.2018.537 Published online by Cambridge University Press

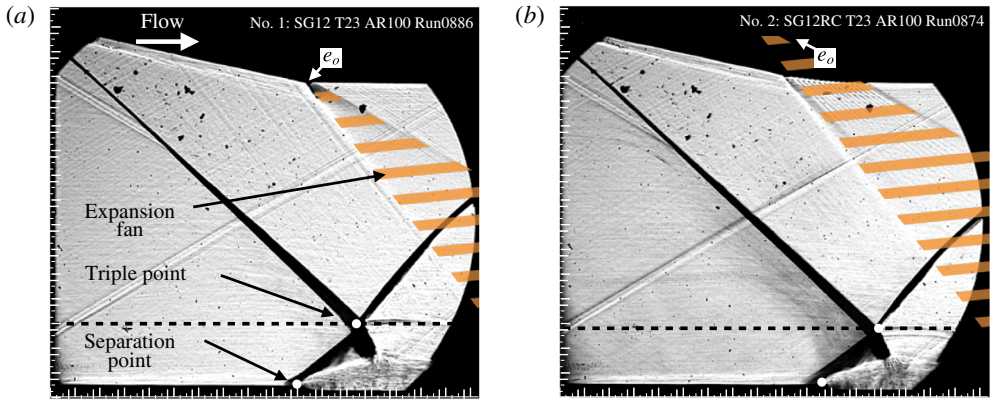

FIGURE 14. (Colour online) Schlieren photographs showing the effect of corner rounding ($M_0 = 2$, $\theta = 12°$, $AR_{eff} = 1.00$, thickness = 23.8 mm): (*a*) no. 1: SG12 T23 straight corner; (*b*) no. 2: SG12RC T23 rounded corner.

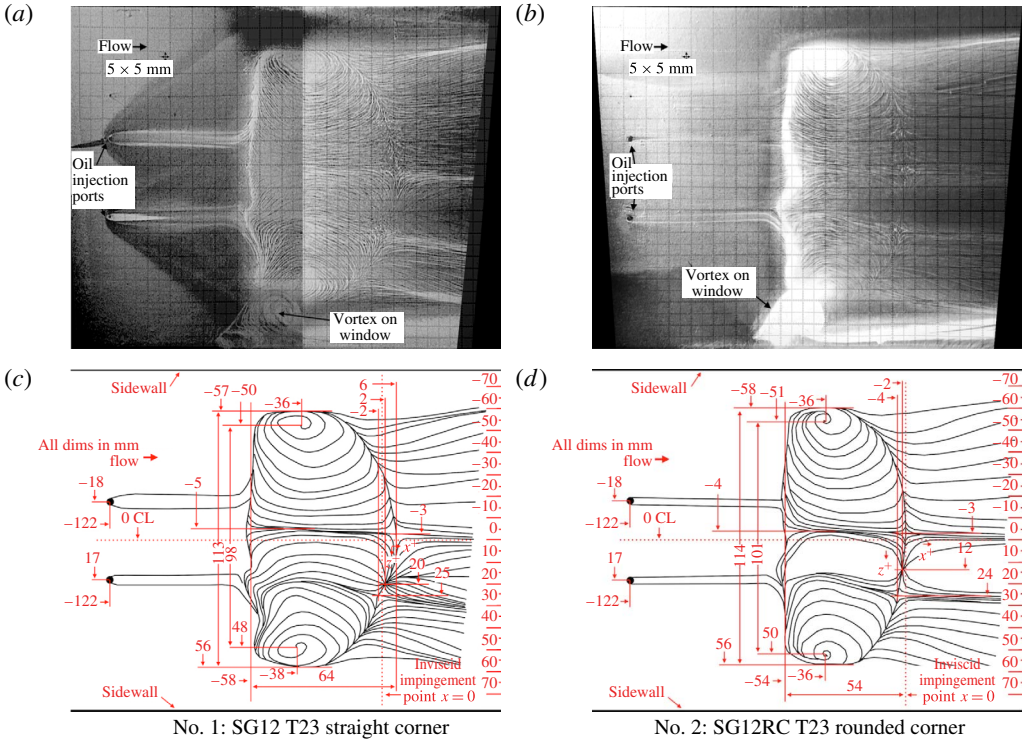

No. 1: SG12 T23 straight corner

No. 2: SG12RC T23 rounded corner

FIGURE 15. (Colour online) Flow separation topology showing the effect of corner rounding on separated region topology ($M_0 = 2$, $\theta = 12°$, $AR_{eff} = 1.00$).

and 13, namely an RR-SWBLI where the triple point height has decreased, the overall size of the SWBLI has decreased and the point of boundary layer separation has moved downstream. Figure 15 shows that the six critical points are present and their arrangement remains largely unchanged, save for the dispersion node, which

https://doi.org/10.1017/jfm.2018.537 Published online by Cambridge University Press

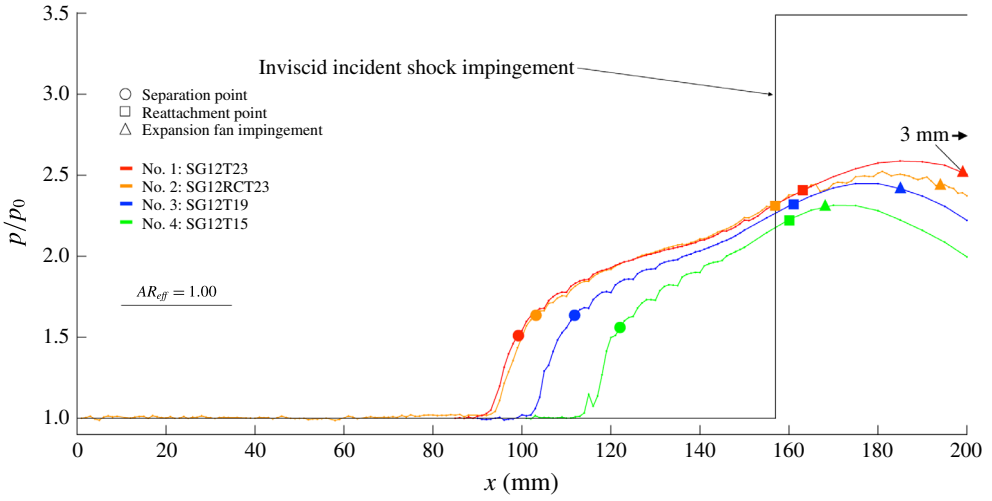

FIGURE 16. (Colour online) Mean normalised static wall pressure distributions with varying shock generator thickness ($M_0 = 2$, $\theta = 12°$, $AR_{eff} = 1.00$).

has shifted towards the centreline by 8 mm. The vortex separation has grown slightly (from 98 to 101 mm) in the rounded corner case, although the separation width is nearly the same (from 113 to 114 mm). The largest change in the topology is the separation length, which has reduced from 64 to 54 mm in the rounded corner case, which is consistent with the trend observed in figure 13.

Figure 16 shows the effect of shock generator thickness and corner rounding on the static pressure distribution through the separated region. All four pressure profiles share the same inviscid incident shock impingement point. The separation and reattachment points obtained from the surface oil flow visualisations along with the approximate first characteristic of the expansion fan impingement are all annotated for each profile. Each profile has varying degrees of spatial resolution due to data acquisition constraints. The lowest spatial resolution for any profile is 5 mm, but all initially feature 1 mm resolution around the point of separation and through most of the separated region.

All four profiles exhibit a uniform inflow pressure followed by a sharp two-step rise across the SWBLI and finally a drop in pressure due to the incident expansion fan. Taking the no. 1: SG12T23 shock generator as a baseline in figure 16, three characteristic changes are observed as the expansion fan impingement point is moved progressively upstream for the test case no. 2: SG12RCT23, followed by nos. 3: SG12T19 and 4: SG12T15. Perhaps the most notable characteristic is that the reattachment points for all three cases appear to remain nearly fixed relative to the baseline case (although the reattachment point for case no. 2: SG12RCT23 shifts upstream slightly). In addition, the separation point moves downstream, effectively reducing the streamwise extent of the pressure rise up to reattachment. Lastly, both the pressure rise to separation and the pressure rise to reattachment change slightly but do not exhibit a clear trend.

All of the profiles exhibit a repeating pattern of concave bumps immediately downstream of the separation point in figure 16. This effect is attributed to the spanwise staggered arrangement of static tappings that was necessary to achieve 1 mm streamwise resolution, an assertion that is supported by the fact that the

https://doi.org/10.1017/jfm.2018.537 Published online by Cambridge University Press

Shock generator	AR_{eff}	L (mm)	L_{sep} (mm)	W_{sep} (mm)	L_{int} (mm)	Triple point height (mm)
No. 1: SG12T23	1.00	45.3	64	113	58	26.3
No. 1: SG12T23	1.35	57.9	76	128	64	29.0/34.8(*MR*)
No. 2: SG12RCT23	1.00	36.5	54	114	54	24.5
No. 2: SG12RCT23	1.25	46.2	67	109	58	27.8/31.1(*MR*)
No. 2: SG12RCT23	1.35	49.1	70	120	60	28.3/31.6(*MR*)
No. 3: SG12T19	1.00	28.0	49	119	45	21.2
No. 3: SG12T19	1.35	40.6	62	117	52	26.2
No. 4: SG12T15	1.00	10.7	38	120	35	14.6
No. 4: SG12T15	1.25	20.3	41	119	36	15.8
No. 4: SG12T15	1.35	23.2	45	113	38	17.0

TABLE 5. Summary of interaction dimensions for all configurations tested (W_{sep} is the separation width).

bumps repeat every 5 mm and are spatially aligned between the different test cases rather than relative to any feature of the pressure profile (e.g. separation point). This illustrates the three-dimensionality inherent in the topology of the separated regions in figures 13 and 15, and hints at a few additional characteristics that are out of the plotted data plane. First, any appearance of this kind of bump is evidence of some variation in the lateral (z-direction) pressure profile. Furthermore, this variation in the lateral pressure profile is not present prior to the initial pressure rise associated with the separated region. For example, the profile in figure 16 for no. 4: SG12T15 shows little spanwise variation until $\approx$115 mm, where a spike is observed. This spike is not an error and is, in fact, indicative of a spanwise pressure mismatch in the region $114 < x < 117$ mm. After the overall initial increase in lateral pressure variation through separation, all four profiles exhibit a reduction of lateral pressure variation as the profiles reach roughly midway between the points of separation and reattachment.

3.5. *The relation between expansion fan position and effective aspect ratio*

In § 3.1, it was seen that SWBLI size, triple point height, separation size and separation length all grow with an increase in AR_{eff}, while in the previous section, it has been shown these same features all grow with an increase in the distance between the expansion fan and the SWBLI. These characteristics are summarised in table 5. To compare these two observed trends, we now attempt to collate the results from all test cases into one plot.

Experiments with the four shock generators seen previously in this study (nos. 1: SG12T23, 2: SG12RCT23, 3: SG12T19 and 4: SG12T15) were conducted at $AR_{eff} = 1.35$ to yield four additional test cases where the upstream first characteristic expansion fan impingement points moved downstream relative to the incident shock inviscid impingement point. This provided four entirely new expansion fan separation cases to compare with those of the previous section. In addition to these eight cases, two additional cases were added by positioning shock generators nos. 2: SG12RCT23 and 4: SG12T15 at $AR_{eff} = 1.25$. Figure 17 conveys the domain for all of the expansion fan impingement points relative to the inviscid incident shock impingement point by aligning all 10 of these cases along their respective inviscid incident shock impingement locations. Key dimensions from figure 17 relating to the expansion fan origin and impingement point for all 10 cases are presented in table 3.

https://doi.org/10.1017/jfm.2018.537 Published online by Cambridge University Press

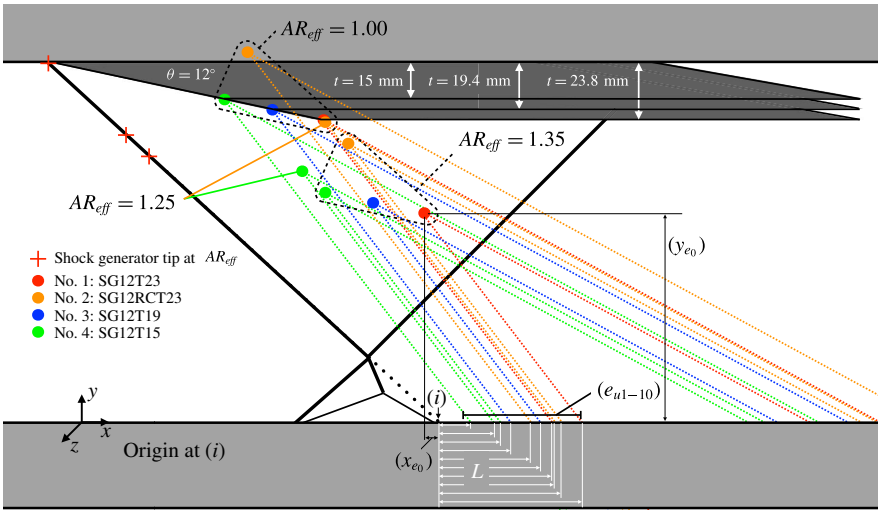

FIGURE 17. (Colour online) Schematic diagram of expansion fan placement with varying thickness and AR_{eff}.

Figure 18 presents the static wall pressure distribution for the low- and high-AR_{eff} test cases. The positions of the separation, reattachment, inviscid incident shock impingement and expansion fan impingement points are all annotated for each pressure profile. In the figure, it can be observed that an increase in AR_{eff} results in an upstream shift of all of the profiles due to the change of the inviscid shock impingement point (117 mm for $AR_{eff} = 1.35$ and 157 mm for $AR_{eff} = 1.00$). However, close inspection reveals that this upstream shift in the profiles is not enough to account for the total movement in the separation point in each profile. Hence, each of the four profiles displays an increase in the streamwise extent that is consistent with the relationship between AR_{eff} and separation length (L_{sep}) previously observed in figure 11.

Figure 18(*b*) presents this information in a line plot aligned on the inviscid shock impingement point. It clearly shows the trend of an increase in the streamwise extent with an increase in shock generator thickness and AR_{eff}. It further demonstrates that the growth of the separated region is accomplished mostly due to an upstream movement in the separation point, with only a relatively small downstream shift in the reattachment points.

The pressure rise to separation at $AR_{eff} = 1.35$ is very similar for all cases, whereas the pressure rise to reattachment progressively grows for all four profiles with the downstream movement of the expansion fan. This is consistent with the concept provided by free interaction theory of splitting the pressure rise at separation from the pressure rise at reattachment, considering the pressure rise to separation to be completely unaffected by the downstream shock or the downstream pressure rise to reattachment. Therefore, if some change has occurred that causes the separation bubble to increase in size, requiring a greater pressure rise to reattachment, the pressure rise to separation will be unchanged and will not contribute to the process. As Délery (2011) explained, the ability for the flow to reattach is directly related to the amount of flow momentum available at the reattachment point, and a shear layer, originating at the separation point, obtains this momentum from the free stream. As

https://doi.org/10.1017/jfm.2018.537 Published online by Cambridge University Press

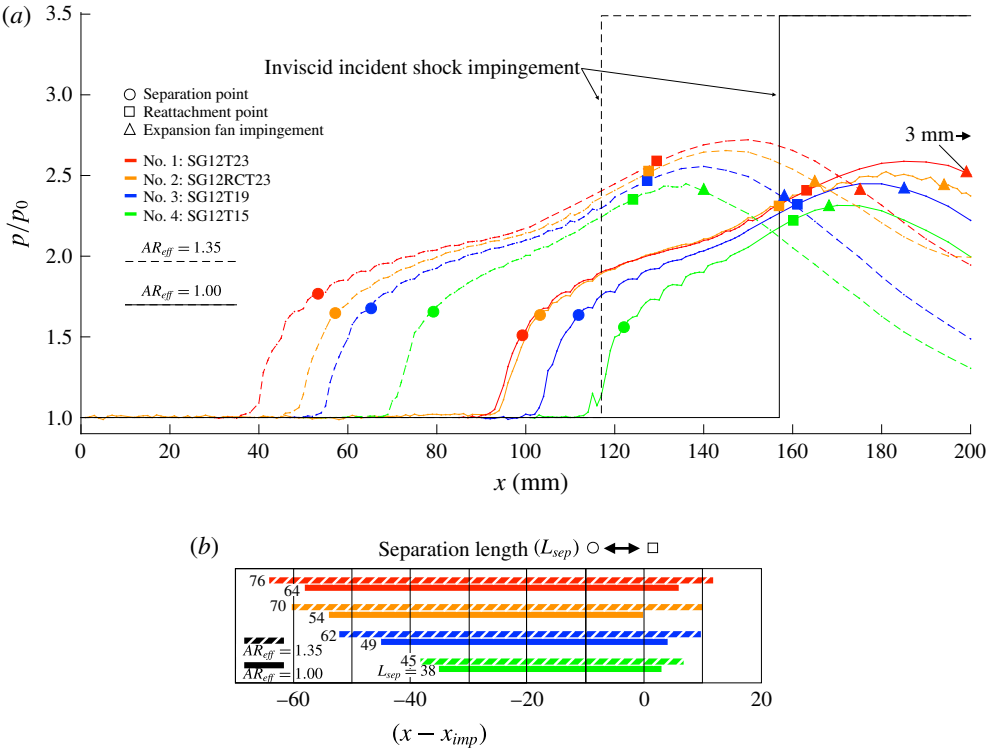

FIGURE 18. (Colour online) (*a*) Mean normalised static wall pressure distributions with varying shock generator thickness and aspect ratio. (*b*) Separation length aligned on the inviscid shock impingement point.

such, if a greater momentum is required at reattachment, the shear layer will need to interact with the free stream over a greater distance, increasing the amount of flow momentum imparted from the free stream. Délery (2011) contended that this is accomplished by a separation point that moves further upstream.

The movement in separation and reattachment points as well as the separation length relative to the distance between the expansion fan impingement point and the inviscid incident shock impingement point are all plotted in figure 19 with accompanying linear regressions. Figure 19(*a*) suggests a direct correlation between expansion fan placement and separation length. Figure 19(*b*) confirms the trend seen in figure 18(*a*), that the growth in separation length is primarily a result of upstream movement of the separation point, in agreement with Délery (2011).

Also of importance and apparent in both figures is that in the range of expansion fan impingement separation (L) investigated, at no point was independence between the expansion fan position and the length of the separated region achieved. Furthermore, the range of L investigated is close to the maximum that could be achieved with the geometries investigated. For example, if the expansion fan were pushed further upstream for the limiting case of no. 4: SG12T15 at $AR_{eff} = 1.00$, the first characteristic of the expansion fan would come into direct contact with the SWBLI. Conversely, if the expansion fan were pushed further downstream for the limiting case of no. 1: SG12T23 at $AR_{eff} = 1.35$, an incident–reflected SWBLI would cease to exist beyond $AR_{eff} = 1.38$ as it would surpass the theoretical limit in this case for a stable

https://doi.org/10.1017/jfm.2018.537 Published online by Cambridge University Press

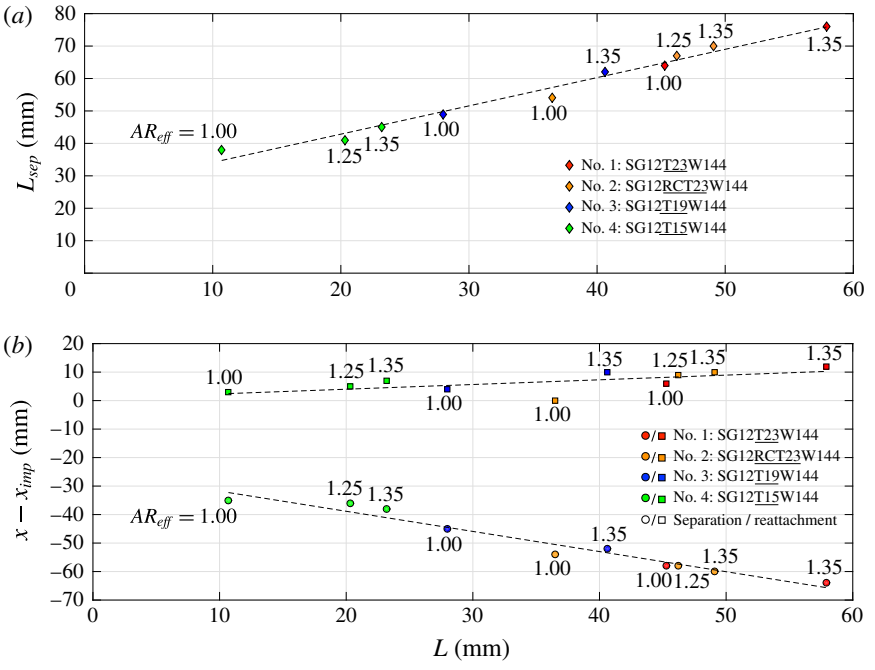

FIGURE 19. (Colour online) Effect of expansion fan impingement separation (L) on (a) separation length (L_{sep}) and (b) incident shock impingement distance ($x - x_{imp}$) of the separation and reattachment points.

shock reflection due to the fact that the reflected shock wave impingement point would have moved far enough upstream to coincide with the expansion fan origin. In the current study, a normal shock wave was observed to form instantaneously at the leading tip in front of the shock generator upon exceeding this limit.

In the past, studies have attempted to reconcile such variations in experimental and numerical data by applying some scaling parameter to a diverse set of reported results. One such study, by Souverein *et al.* (2013), attempted to quantify the variation of interaction length with shock strength, Mach number, geometry and Reynolds number. This scaling analysis introduced by Souverein *et al.* (2013) only depends on the free-stream Mach number and flow deflection angle, given by

$$S_e^* = k\frac{\Delta P}{q_0}, \tag{3.1}$$

where ΔP is the shock intensity, q_0 is the dynamic pressure and k is a constant chosen such that it is one at the onset of separation. In addition to this, Souverein *et al.* (2013) derived a scaled interaction length, given by

$$L^* = \frac{L_{int}}{\delta_c^*} G_3(M_0, \theta) \tag{3.2}$$

and

$$G_3(M_0, \theta) = \frac{\sin(\beta)\sin(\theta)}{\sin(\beta - \theta)}. \tag{3.3}$$

https://doi.org/10.1017/jfm.2018.537 Published online by Cambridge University Press

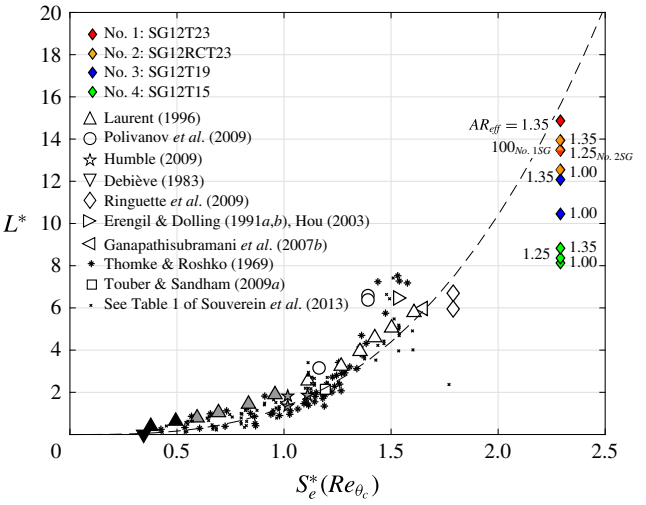

FIGURE 20. (Colour online) Interaction length and shock strength scaling across ramp and incident–reflected interactions of varying Mach and Reynolds numbers (based on compressible momentum thickness) from Souverein *et al.* (2013) for separated (open), incipient (grey) and attached (black) SWBLIs. The dashed line is a best fit line ($a * x^b$, where $a = 1.3$, $b = 3$). The reader is referred to the paper by Souverein *et al.* (2013) for full details of the references that the experimental data are taken from.

The scaled interaction length (L^*) is a function of the free-stream Mach number (M_0), flow deflection angle (θ), compressible displacement thickness (δ_c^*) and length of the interaction (L_{int}), which Souverein *et al.* (2013) define as the distance between the mean location of the separation shock foot and the inviscid incident shock impingement point. Thus, it should be pointed out that L_{int} differs from the separation length L_{sep} discussed above, and for all of the cases in this study, $L_{int} \leqslant L_{sep}$ (see table 5).

When the scaled interaction length is taken together with S_e^*, this enables Souverein *et al.* (2013) to classify the separation states over a range of interactions of varying strength, Mach and Reynolds numbers created by both ramp and incident–reflected SWBLIs. This range of interactions appears grouped in figure 20 for $S_e^* < 2.0$. It can be seen in the figure that almost all of the various studies ($S_e^* < 2.0$) collapse well onto a trend line when quantified by these two scaled parameters. Souverein *et al.* (2013) contended that the remaining scatter of the studies $S_e^* < 2.0$ is largely due to differences in experimental set-up. Since the range of L obtained in the present study represents nearly the full range achievable given the free-stream conditions and flow deflection angle investigated, the results presented here are uniquely positioned to give an estimate of the bounds of the observed scatter in the study of Souverein *et al.* (2013).

The results from the present study appear in figure 20 grouped along a line through $S_e^* = 2.47$ and spread across $15.29 < L^* < 27.95$. These values of S_e^* and L^* greatly expand the envelope of the plot farther than any of the studies considered by Souverein *et al.* (2013). This observed scatter of the data from this study when plotted against the model suggests the following. (1) Expansion fan placement, relative to the SWBLI, has a significant effect on the scatter in the model. The result that lies closest to the model trend line corresponds with the test case that features the greatest

https://doi.org/10.1017/jfm.2018.537 Published online by Cambridge University Press

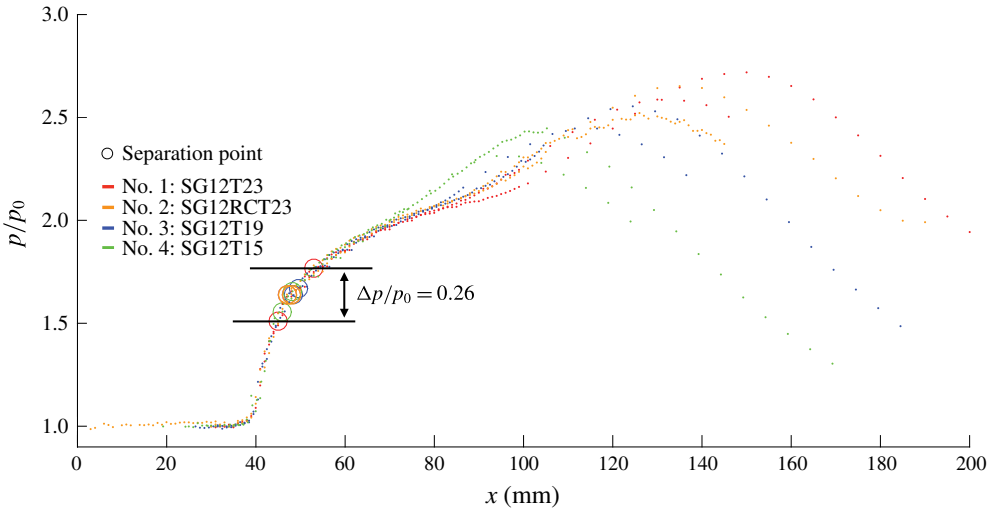

FIGURE 21. (Colour online) Mean normalised static wall pressure distributions of varying thickness and aspect ratio aligned on initial pressure rise to separation.

separation between the expansion fan and the SWBLI. This results in a trend that correlates the closeness of the expansion fan to the SWBLI with a departure from the model trend line of Souverein *et al.* (2013). (2) Since the range of expansion fan placement (L) represents nearly the full range possible, the observed scatter of the data from this study may be, to the first order, a good approximation of the bounds of scatter within the model.

It should be noted that a value of $k = 2.5$ was used based upon the criteria outlined by Souverein *et al.* (2013), but that the Reynolds number of this study ($Re_\theta = 10124$; see table 1) lies significantly close to the switch criterion between the two values of k. In addition to this, incorporation of the data from the present study requires a relatively long-range extrapolation of the trend line of Souverein *et al.* (2013), which is in itself a significant source of uncertainty.

3.6. *Free interaction theory*

The free interaction theory of Chapman *et al.* (1958) states that the initial pressure rise to the point of boundary layer separation is governed solely by the flow properties at the onset of separation and is thus independent of the overall configuration or the agency through which separation is induced. This suggests that the pressure profiles taken at various AR_{eff} and with different shock generator thicknesses should all exhibit near identical initial pressure rises to separation. To compare the initial SWBLI-induced pressure rise of each of the profiles in figure 18, they have been replotted in figure 21, aligned so as to match the initial pressure rise of the no. 1: SG12T23 $AR_{eff} = 1.35$ case.

Figure 21 shows that all eight profiles do indeed follow an almost identical initial pressure rise up to the point of separation, after which they begin to diverge. However, the points of separation for each configuration are not identical, instead being spread over a range of 8 mm in streamwise extent and occurring at pressures in the range $0.182 < p/p_t < 0.213$. This compares with the theoretical value of 0.198 proposed

https://doi.org/10.1017/jfm.2018.537 Published online by Cambridge University Press

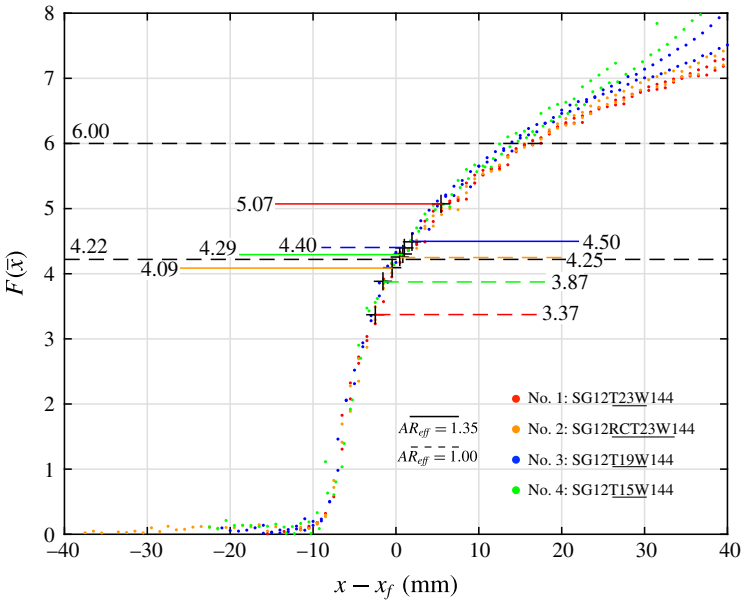

FIGURE 22. (Colour online) Universal correlation function evaluated for nos. 1: SG12T23, 2: SG12RCT23, 3: SG12T19 and 4: SG12T15; $AR_{eff} = 1.00$–1.35.

by Erdos & Pallone (1962), who suggested that the pressure rise during the free interaction process is governed by

$$\frac{p - p_0}{q_0} = F(\bar{x})\sqrt{\frac{2\ C_f}{(M_0^2 - 1)^{1/2}}}, \tag{3.4}$$

where the universal correlation function $F(\bar{x})$ is defined by

$$F(\bar{x}) = \sqrt{f_1(\bar{x}) f_2(\bar{x})}, \tag{3.5}$$

where

$$f_1(\bar{x}) = \int_{\bar{x}_0}^{\bar{x}} \left(\frac{\partial \bar{\tau}}{\partial \bar{y}}\right)_w \mathrm{d}\bar{x}, \quad f_2(\bar{x}) = \frac{\mathrm{d}\bar{\delta}_0^*}{\mathrm{d}\bar{x}}, \quad \bar{\tau} = \frac{\tau}{\tau_{w0}}, \quad \bar{y} = \frac{y}{\delta_0^*}, \quad \bar{x} = \frac{x - x_0}{L_{rise}}. \tag{3.6a,b}$$

Here, τ is the shear stress, τ_{w0} is the wall shear stress at the interaction origin (x_0), δ_0^* is the boundary layer displacement thickness and L_{rise} is the length characteristic of the streamwise extent of free interaction.

In figure 22, the universal correlation function $F(\bar{x})$ is evaluated for all eight cases of figure 21. Annotated on the figure with dashed lines are the values of $F(\bar{x})$ at separation for each of the cases as well as the values proposed by Erdos & Pallone (1962) for $F(\bar{x})_{separation} = 4.22$ and $F(\bar{x})_{plateau} = 6.00$ for a turbulent flow. The reference point x_f in figure 22 is defined as the location on the curves where $F(\bar{x}) = 4.22$.

Taking all profiles into account, the experimentally determined average value of $F(\bar{x})_{separation}$ for this study is 4.23, in close agreement with the value $F(\bar{x})_{separation} = 4.22$ proposed by Erdos & Pallone (1962). However, due to the relatively low strength of the interaction (i.e. pressure ratio), no meaningful pressure profile plateau was observed for any of the profiles in figure 22, and thus no experimentally determined values are annotated.

https://doi.org/10.1017/jfm.2018.537 Published online by Cambridge University Press

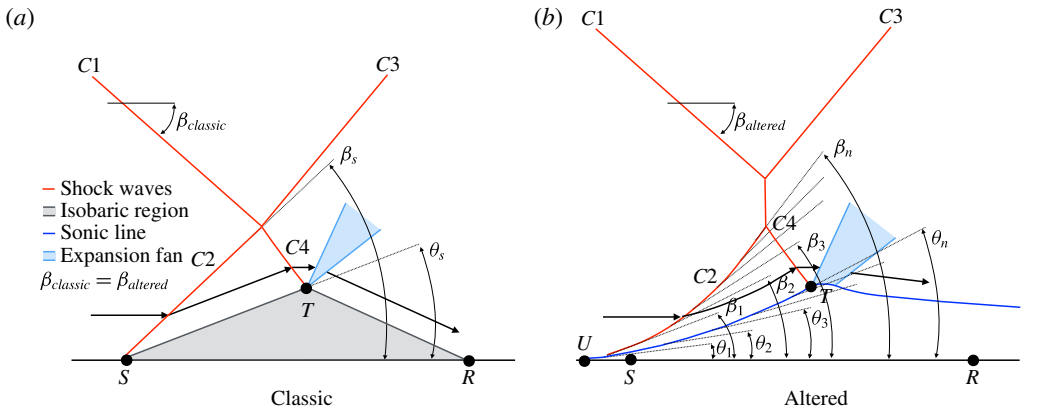

FIGURE 23. (Colour online) Classic inviscid model for incident–reflected SWBLI and an altered representation.

3.7. *Discussion of separation shock characteristics*

In the numerical study of Matheis & Hickel (2015), it was observed that in an $M_0 = 2$ flow, if the flow deflection angle was increased (and thus the incident shock strength) beyond $\theta = 11°$, the mean separation shock angle remained nearly constant. Matheis & Hickel (2015) also contended that this behaviour is characteristic of the free interaction theory of Chapman *et al.* (1958).

In the present study, an RR-SWBLI is observed for $\theta = 12°$ at low AR_{eff}, while an MR-SWBLI is observed at high AR_{eff}, with the incident flow deflection held constant, and thus the strength of the incident oblique shock wave. From this, we reasonably conclude that the only mechanism for a sustained transition to MR is through an increase in the mean separation shock angle. To address this apparent contradiction between the results of this study and those of Matheis & Hickel (2015), we discuss the classic inviscid model for an incident–reflected SWBLI and propose a slightly altered representation that is consistent with the results seen in the previous sections.

The 'classic' inviscid model for an incident–reflected SWBLI with separation appears in figure 23. The isobaric shock-induced separated region *S*–*T*–*R* is modelled as a physical obstruction requiring a sharp flow deflection much like a physical ramp. The sonic line of the boundary layer in a viscous model could serve as an acceptable proxy for the border of region *S*–*T*–*R*, such that outside of this region the flow is supersonic, allowing for the formation of shock waves. The separation shock angle (β_s) would then be dictated by the angle (θ_s) of the upstream face of the isobaric region, modelled as a straight line *S*–*T*, turning the flow parallel with this line, travelling unhindered until it reaches the transmitted shock (*C*4) and an expansion fan, which turns the flow over the crest of the isobaric separated region. The idealised pressure profile of the classic model would feature a two-step pressure rise: one sharp pressure rise at point *S* and another sharp pressure rise at point *R*, with a plateau region between points *S* and *R* through the isobaric separated region.

In reality, as seen in figures 11, 13 and 15, the separated region is in fact a highly three-dimensional region with significant streamwise and stream-normal variations even in a time-averaged sense. When time is taken into account, it is known that the separated region exhibits even greater variation. For example, Touber & Sandham (2009) observed displacement of the separation and reattachment points

https://doi.org/10.1017/jfm.2018.537 Published online by Cambridge University Press

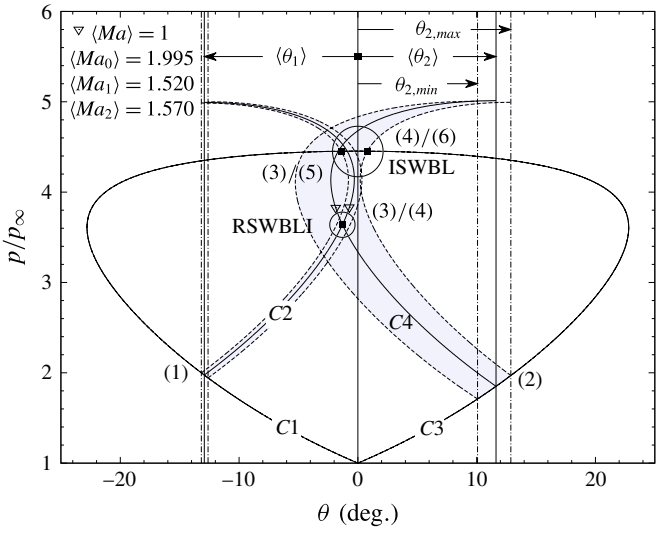

FIGURE 24. (Colour online) Shock polar for $\theta = 13°$ exhibiting separation shock variance from Matheis & Hickel (2015) (notation altered for consistency).

over time as well as the breaking up and enhancement of the upstream section of the separation bubble, inducing translation and rotation in the separation shock. Matheis & Hickel (2015) observed that the separation shock angle fluctuated in the range of $\beta = 39.50°$–$42.74°$ for their $\theta = 13°$ case, and attributed this to the fluctuations and inherent dynamics of the incoming turbulent boundary layer. The net result of this fluctuation in time of the separation shock angle and the relationship it has with the SWBLI as a whole can be better understood from the shock polar representation in figure 24 for the $\theta = 13°$ case. In the figure, the separation shock polar originating from point 2 at $\theta \approx 11.4°$ is observed to grow and shrink with time. At some points in time, the two polars overlap and RR-SWBLI is observed, while at other points in time, the two polars pull apart and MR-SWBLI is observed. In the present study, when the arrangement of the shock generator AR_{eff} and expansion fan placement is such as to allow for an MR-SWBLI to occur, it is likely that this fluctuation in time of the separation shock angle is the mechanism that triggers transition from RR-SWBLI to MR-SWBLI. Indeed, similar observations were made in the present study for the $\theta = 12°$ cases from the schlieren video taken, particularly in intermediate AR_{eff} around the point of transition. However, for reasons just discussed, it is difficult to assign a particular AR_{eff} to the transition point as, over a range of intermediate AR_{eff}, multiple transitions between RR-SWBLI and MR-SWBLI exist. It is important to reassure the reader, in light of this uncertainty, that the observed RR-SWBLI at low AR_{eff} and the observed MR-SWBLI at high AR_{eff} in the $\theta = 12°$ case are not transient and represent an average state change for the SWBLI. Evidence of this is provided in § 3.1 in figures 9(*c*) and 9(*d*), which clearly show RR-SWBLI at $AR_{eff} = 1.00$ and MR-SWBLI at $AR_{eff} = 1.38$ and are ensemble averages over 3.8 s.

Furthermore, as mentioned in § 1.3, it is widely known that the inclusion of sidewalls can have large three-dimensional effects on the resulting flow (Bruce *et al.* 2011; Burton & Babinsky 2012; Babinsky *et al.* 2013; Benek *et al.* 2013; Galbraith *et al.* 2013; Wang *et al.* 2015). We content that so-called three-dimensional effects, such as pressure disturbances generated by viscous flow phenomena in the

https://doi.org/10.1017/jfm.2018.537 Published online by Cambridge University Press

tunnel corners, as reported by Babinsky *et al.* (2013), may also contribute to the 'non-canonical' development of the separation bubble (and hence separation shock) at the tunnel centreline. The presence of additional compressive waves at the centreline downstream of the separation point would be consistent with a steepening of the front shock leg and an increase in the angle of flow separation. This is in contrast to the study of Matheis & Hickel (2015), which featured periodic boundary conditions and thus would not have these three-dimensional effects generated by corners.

Taking all of this into account, it is clear that the separation shock is dictated by the nature of a highly variable (in space and time) separated region and that the upstream facing section of the separated region *S*–*T* is unlikely to be a straight line, as in the classic inviscid model, and is more likely to exhibit some amount of curvature at one or many points and will change over time. These concepts are not new and can be regarded as widely accepted. However, the appreciation of these concepts with regard to transition helps to explain the results seen in this study. Thus, a representation that incorporates these concepts appears in figure 23, labelled 'altered'. In this representation, there exists shock-induced flow separation somewhere in the region of *S*–*T*–*R*, which causes the sonic line to navigate up and around it and has a limited upstream influence as far as point *U*. The supersonic flow above the sonic line that must navigate the obstruction posed by the separated region is turned by a separation shock. As the line *U*–*T* is not straight (it has been exaggerated for clarity), there exists not one value of θ but many values θ_1–θ_n progressively requiring the flow to turn by a greater amount. This flow turning will naturally occur through a separation shock β, but, as there are many values of θ, there will be many values of β, and thus the separation shock will progressively turn β_1–β_n. This line has been drawn concave, but this is arbitrary, and it could be drawn convex, or any combination thereof. In this representation, β_1 could be small enough to permit RR-SWBLI, but here β_n could have exceeded the maximum turning angle of the flow as required by the region immediately downstream of shock *C*3, resulting in MR-SWBLI.

If the time-average separation shock angle is dependent upon the entire time-averaged upstream facing section of the separation bubble (line *U*–*T*), then for free interaction theory to dictate its mean angle, it would also need to dictate the entire line *U*–*T*. This is possible for strong interactions. However, in this study, as mentioned in the previous section, no pressure plateau was observed for any of the interactions due to the relative weakness of the interaction. In this case, free interaction theory is only applicable up to the point of separation. This range of influence across the altered representation is presented in figure 25. In this figure, it can be seen that the separation shock influence region *U*–*T* and the free interaction region *U*–*S* overlap, but that most of the separation shock influence region remains out of range of free interaction theory. Therefore, free interaction theory may be responsible for some initial contributions to the separation shock, as indicated in the figure for θ_1 and β_1. However, it is unlikely that the rest of the line *S*–*T*, and with it θ_2–θ_n and β_2–β_n, would be dependent upon free interaction theory, leaving the majority of the separation shock to be dependent upon the separation bubble as a whole, which can be affected by two-dimensional effects (e.g. expansion fan proximity), three-dimensional effects (e.g. sidewalls, corner effects and aspect ratio) and unsteady effects (e.g. incoming turbulent boundary layer).

4. Conclusions

The results from a novel experimental set-up to vary the effective aspect ratio of a fixed aspect ratio wind tunnel were presented, demonstrating transition between an RR

https://doi.org/10.1017/jfm.2018.537 Published online by Cambridge University Press

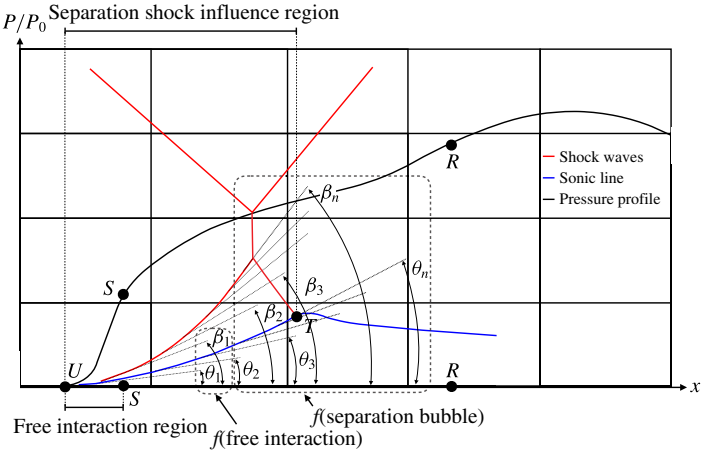

FIGURE 25. (Colour online) Extent to which free interaction theory affects separation shock development.

and an irregular reflected (MR) SWBLI without an increase in incident shock strength or flow deflection. Several shock generators of varying geometry, but all featuring a fixed flow deflection angle of 12°, were tested in an $M_0 = 2$ flow at a range of effective aspect ratios ($AR_{eff} = 1.00$–1.38). Features of the resulting SWBLI were visualised and quantified through the use of schlieren photography, PIV, surface oil flow visualisation and high-spatial-resolution static pressure measurements.

In § 3.1, it was observed through schlieren photography that an increase in AR_{eff} from 1.00 to 1.38 resulted in an SWBLI evolution from an Edney type I interference (RR-SWBLI) to an Edney type II interference (MR-SWBLI), with an associated onset of MR. This evolution was confirmed in a time-averaged sense in § 3.3 through the use of PIV, which also made it possible to measure the average separation shock angles and to produce shock polars for the two states. Surface flow visualisations revealed the critical point topology of the separated flow regions, giving insight into the three-dimensionality of the flow. An increase in the streamwise extent of the shock-induced boundary layer separation was observed with an increase in AR_{eff}. It was also seen that the arrangement of the critical point topology changes with an increase in AR_{eff}. This change in critical point topology in turn sees the streamwise separation lengths grow proportionally with AR_{eff}.

The transition from RR-SWBLI to MR-SWBLI with an increase in AR_{eff} and a fixed flow deflection angle raised two questions. The first concerns the role of the downstream expansion fan and the upstream propagation of information due to the fact that increasing AR_{eff} alters the relative orientation of the SWBLI and the expansion fan. Second, it was observed in the study of Matheis & Hickel (2015) that the time-averaged separation shock angle was constant for flow deflections $\theta > 11°$ in an $M_0 = 2$ flow. Furthermore, it was concluded by Matheis & Hickel (2015) that this was characteristic of the free interaction theory of Chapman *et al.* (1958), which, if applicable, would seemingly prohibit any transition from RR-SWBLI to MR-SWBLI with a fixed flow deflection.

In § 3.4, the role of the expansion fan was investigated in detail through the use of additional shock generators. Each shock generator featured a different thickness or corner rounding which respectively physically or virtually shifted the sharp corner

https://doi.org/10.1017/jfm.2018.537 Published online by Cambridge University Press

of the shock generator, enabling a systematic investigation of their effects. It was observed that with a downstream movement of the expansion fan, SWBLI size, triple point height, separation size, separation length and static pressure distribution all grew. The relationship between AR_{eff} and expansion fan placement was further investigated in § 3.5. It was observed that the centreline separation length grew linearly with an increase in separation between the SWBLI and the expansion fan, and that the growth in the separated region was accommodated primarily by an upstream movement of the separation point, with the reattachment point remaining almost fixed for $AR_{eff} = 1.00$–1.35. Furthermore, no independence of the SWBLI from the placement of the expansion fan was observed for the entire range of placements achievable in this experiment. This conclusion raises important questions about the influence of such 'secondary' geometric features of an experimental set-up, which, more often than not, are not fully considered or go completely unreported. Further investigation through experiments with test cases that provide a greater achievable range of expansion fan placement, which could only be accomplished with shock generators featuring lower flow deflection angles and/or tests at higher Mach numbers, may help to better understand the upstream expansion fan influence on SWBLIs.

In § 3.6, the applicability of free interaction theory with respect to the pressure rise to separation was observed. However, due to the relative weakness of the interaction, no pressure profile plateau was observed in any of the test cases. In light of this, an SWBLI representation was presented and reasoned in § 3.7, which explained the observed results, suggesting that for the weak interaction observed in this study, free interaction theory, while contributing to the definition of the mean separation shock angle, does not prohibit the vast majority of the mean separation shock from being influenced by the separation bubble as a whole, including any downstream factors.

Acknowledgements

The first author gratefully acknowledges the support of the Imperial College President's PhD Scholarship Scheme, supported by the EPSRC, for funding this research.

REFERENCES

AGOSTINI, L., LARCHEVEQUE, L. & DUPONT, P. 2015 Mechanism of shock unsteadiness in separated shock/boundary-layer interactions. *Phys. Fluids* **27**, 126103.

BABINSKY, H. & OGAWA, H. 2008 SBLI control for wings and inlets. *Shock Waves* **18** (2), 89–96.

BABINSKY, H., OOREBEEK, J. & COTTINGHAM, T. G. 2013 Corner effects in reflecting oblique shock-wave/boundary-layer interactions. In *51st AIAA Aerospace Sciences Meeting including the New Horizons Forum and Aerospace Exposition 07–10 January 2013, Grapevine, Texas*, pp. 1–10. American Institute of Aeronautics and Astronautics.

BEN-DOR, G. 2007 *Shock Wave Reflection Phenomena*, 2nd edn. Springer.

BENEK, J. A., SUCHYTA, C. J. III & BABINSKY, H. 2013 The effect of wind tunnel size on incident shock boundary layer interaction experiments. In *51st AIAA Aerospace Sciences Meeting including the New Horizons Forum and Aerospace Exposition 07–10 January 2013, Grapevine, Texas*, pp. 1–24. American Institute of Aeronautics and Astronautics.

BRUCE, P. J. K., BURTON, D. M. F., TITCHENER, N. A. & BABINSKY, H. 2011 Corner effect and separation in transonic channel flows. *J. Fluid Mech.* **679**, 247–262.

BURTON, D. M. F. & BABINSKY, H. 2012 Corner separation effects for normal shock wave/turbulent boundary layer interactions in rectangular channels. *J. Fluid Mech.* **707**, 287–306.

https://doi.org/10.1017/jfm.2018.537 Published online by Cambridge University Press

CHAPMAN, D. R., KUEHN, D. M. & LARSON, H. K. 1958 Investigation of separated flows in supersonic and subsonic streams with emphasis on the effect of transition. NACA *Tech. Rep.* 1356.

CHPOUN, A., PASSEREL, D., LI, H. & BEN-DOR, G. 1995 Reconsideration of oblique shock wave reflections in steady flows. Part 1. Experimental investigation. *J. Fluid Mech.* **301**, 19–35.

CONCORDE-SST 2002 http://www.concordesst.com/model101/taster/sd4.jpg.

DAPM 2016 http://daytonipms.com/walks/F-15E/PortEngineIntake.jpg.

DÉLERY, J. 2011 Physical introduction. In *Shock Wave–Boundary-Layer Interactions*, Ist edn. (ed. H. Babinsky & J. K. Harvey). Cambridge University Press.

DÉLERY, J. M., MARVIN, J. G. & RESHOTKO, E. 1986 Shock-wave boundary layer interactions. *Tech. Rep.* AGARD-AG-280. North Atlantic Treaty Organization Advisory Group for Aerospace Research and Development. National Technical Information Services.

EDNEY, B. 1968 Anomalous heat transfer and pressure distributions on blunt bodies at hypersonic speeds in the presence of an impinging shock. *Tech. Rep.* FFA Report 115. Aeronautical Research Institute of Sweden, Stockholm.

ERDOS, J. & PALLONE, A. 1962 Shock–boundary layer interaction and flow separation. In *Proceedings of the 1962 Heat Transfer and Fluid Mechanics Institute,* vol. 15, pp. 239–254. Stanford University Press.

GALBRAITH, D. S., TURNER, M. G., ORKWISR, P. D. & WEIL, S. P. 2013 The effect of aspect ratio on a Mach 2.75 shock boundary layer interaction configuration. In *51st AIAA Aerospace Sciences Meeting including the New Horizons Forum and Aerospace Exposition 07–10 January 2013, Grapevine, Texas*, pp. 1–12. American Institute of Aeronautics and Astronautics.

GANAPATHISUBRAMANI, B., CLEMENS, N. T. & DOLLING, D. S. 2009 Low-frequency dynamics of shock-induced separation in a compression ramp interaction. *J. Fluid Mech.* **636**, 397–425.

HENDERSON, L. F. 1967 The reflexion of a shock wave at a rigid wall in the presence of a boundary layer. *J. Fluid Mech.* **30** (4), 699–722.

HENDERSON, L. F. & LOZZI, A. 1975 Experiments on transition of Mach reflection. *J. Fluid Mech.* **68** (1), 139–155.

HORNUNG, H. G., OERTEL, H. & SANDEMAN, R. J. 1979 Transition to Mach reflexion of shock waves in steady and pseudosteady flow with and without relaxation. *J. Fluid Mech.* **90** (3), 541–560.

HORNUNG, H. G. & ROBINSON, M. L. 1982 Transition from regular to Mach reflection of shock waves. Part 2. The steady-flow criterion. *J. Fluid Mech.* **123**, 155–164.

LI, H. & BEN-DOR, G. 1997 A parametric study of Mach reflection in steady flows. *J. Fluid Mech.* **341**, 101–125.

LI, H., CHPOUN, A. & BEN-DOR, G. 1999 Analytical and experimental investigations of the reflection of asymmetric shock waves in steady flows. *J. Fluid Mech.* **390**, 25–43.

LOCK, G. & DEWEY, J. 1989 An experimental investigation of the sonic criterion for transition from regular to Mach reflection of weak shock waves. *Exp. Fluids* **7** (5), 289–292.

LONGLEY, J. P. & GREITZER, E. M. 1992 Inlet distortion effects in aircraft propulsion system integration. In *AGARD, Steady and Transient Performance Prediction of Gas Turbine Engines; 18 p*, pp. 1–18. National Technical Information Services.

LOTH, E., TITCHENER, N., BABINSKY, H. & POVINELLI, L. 2013 Canonical normal shock wave/boundary-layer interaction flows relevant to external compression inlets. *AIAA J.* **51** (9), 2208–2217.

MATHEIS, J. & HICKEL, S. 2015 On the transition between regular and irregular shock patterns of shock-wave/boundary-layer interactions. *J. Fluid Mech.* **776**, 200–234.

VON NEUMANN, J. 1943*a* Oblique reflection of shocks. *Explosive Research Rep.* 12. Navy Department, Bureau of Ordnance.

VON NEUMANN, J. 1943*b* Refraction, intersection and reflection of shock waves. *NAVORD Rep.* 203-45. Navy Department, Bureau of Ordnance.

OGAWA, H. & BABINSKY, H. 2006 Wind-tunnel setup for investigations of normal shock wave/boundary layer interaction control. *AIAA J.* **44** (11), 2803–2805.

https://doi.org/10.1017/jfm.2018.537 Published online by Cambridge University Press

PERRY, A. E. & CHONG, M. S. 1987 A description of eddying motions and flow patterns using critical-point concepts. *Annu. Rev. Fluid Mech.* **19** (1), 125–155.

PIPONNIAU, S., DUSSAUGE, J. P., DEBIEVE, J. F. & DUPONT, P. 2009 A simple model for low-frequency unsteadiness in shock-induced separation. *J. Fluid Mech.* **629**, 87–108.

RABEY, P. K. & BRUCE, P. J. K. 2017 Experimental study exploring unsteadiness length scales in a reflected shock–boundary layer interaction. In *55th AIAA Aerospace Sciences Meeting, AIAA SciTech Forum, Grapevine, Texas*, pp. 1–14. American Institute of Aeronautics and Astronautics.

SMART, M. K. 2001 Experimental testing of a hypersonic inlet with rectangular-to-elliptical shape transition. *J. Propul. Power* **17** (2), 276–283.

SOUVEREIN, L. J., BAKKER, P. G. & DUPONT, P. 2013 A scaling analysis for turbulent shock-wave/boundary-layer interactions. *J. Fluid Mech.* **714**, 505–535.

THREADGILL, J. A. S. & BRUCE, P. J. K. 2016 Shock wave boundary layer interaction unsteadiness: the effects of configuration and strength. In *54th AIAA Aerospace Sciences Meeting, AIAA SciTech Forum, San Diego, CA*, pp. 1–19. American Institute of Aeronautics and Astronautics.

THREADGILL, J. A. S. & BRUCE, P. J. K. 2017 Comparison of unsteady flow similarities in various shock/boundary-layer interaction configurations. In *55th AIAA Aerospace Sciences Meeting, AIAA SciTech Forum, Grapevine, Texas*, pp. 1–17. American Institute of Aeronautics and Astronautics.

TOUBER, E. & SANDHAM, N. D. 2008 Oblique shock impinging on a turbulent boundary layer: low-frequency mechanisms. In *38th Fluid Dynamics Conference and Exhibit, Seattle, Washington*, pp. 1–27. American Institute of Aeronautics and Astronautics.

TOUBER, E. & SANDHAM, N. D. 2009 Large-eddy simulation of low-frequency unsteadiness in a turbulent shock-induced separation bubble. *Theor. Comput. Fluid Dyn.* **23** (2), 79–107.

TOUBER, E. & SANDHAM, N. D. 2011 Low-order stochastic modelling of low-frequency motions in reflected shock-wave/boundary-layer interactions. *J. Fluid Mech.* **671**, 417–465.

VUILLON, J., ZEITOUN, D. & BEN-DOR, G. 1995 Reconsideration of oblique shock wave reflections in steady flows. Part 2. Numerical investigation. *J. Fluid Mech.* **301**, 37–50.

WANG, B., SANDHAM, N. D., HU, Z. & LIU, W. 2015 Numerical study of oblique shock-wave/boundary-layer interaction considering sidewall effects. *J. Fluid Mech.* **767**, 526–561.

https://doi.org/10.1017/jfm.2018.537 Published online by Cambridge University Press